Deformation and strain limits for IPB-loaded high strength steel CHS joints

Kim, Seon Hu; Lee, Cheol Ho; Han, Sang Hui; Wardenier, Jaap

DOI
10.1016/j.tws.2022.109681

Publication date
2022

Document Version
Final published version

Published in
Thin-Walled Structures

Thin-Walled Structures 179 (2022) 109681

Contents lists available at ScienceDirect

Thin-Walled Structures

journal homepage: www.elsevier.com/locate/tws

Full length article

Deformation and strain limits for IPB-loaded high strength steel CHS joints

Seon-Hu Kim [a], Cheol-Ho Lee [a,*], Sang-Hui Han [b], Jaap Wardenier [c]

[a] Department of Architecture and Architectural Engineering, Seoul National University, Seoul 08826, South Korea
[b] Dongyang Structural Engineers Group, Seoul 05836, South Korea
[c] Faculty of Civil Engineering and Geosciences, Delft University of Technology, 2600GA Delft, The Netherlands

ARTICLE INFO

Keywords:
Circular hollow section (CHS)
Deformation limit
Experiment
Finite element (FE)
High-strength steel
Hollow section joint
In-plane bending (IPB)

ABSTRACT

In this study, existing deformation limits are first re-examined to investigate if they can be rationally extended to high strength steel circular hollow section (CHS) joints that are subjected to in-plane bending (IPB) moment. It is pointed out that existing deformation limits, which have been developed and validated primarily for mild steel joints, need to be modified when high strength steels are involved. By noting that the ductility of IPB-loaded joints can be significantly reduced with the use of high strength steel, a new deformation limit is proposed which allows less deformation to less ductile high strength steel joints. The deformation limit, proposed in terms of joint rotation angle, is validated both numerically and experimentally. In addition, a recently proposed strain limit criterion is also discussed. To provide a guide for obtaining converged strain from finite element (FE) analysis, mesh sensitivity study is comprehensively conducted. It is shown that the element size required for the convergence of strain is substantially smaller than that required for obtaining satisfactory global response such as joint load-deformation relationship. By applying a systematic FE modeling strategy, numerical investigation is made to check the feasibility of the 5% strain limit criterion which has recently been advocated by the revised draft of ISO 14346. While the limiting principal strain of 5% is shown to be reasonable for CHS-to-CHS joints loaded by IPB, for longitudinal branch plate-to-CHS joints, a lower limiting strain appears more appropriate.

1. Introduction

Because many tubular joints are flexible and the local joint deformation is often non-negligible, the load-bearing capacity of a tubular joint should be limited by a well-established deformation limit. From the joint load-deformation relationship, the ultimate strength is determined as the preceding one between the first peak load and the load corresponding to a prescribed deformation limit, as illustrated in Fig. 1(a). According to the CIDECT design guides [1,2], the "3%" local deformation of the chord dimension has been recommended as the limiting value; 3% of the chord diameter for circular hollow section (CHS) joints and 3% of the chord width for rectangular hollow section (RHS) joints.

Although the 3% limit was originally suggested based on the numerical analysis of mild steel tubular joints [3], the same 3% limit has also been frequently employed to high strength steel joints in determination of their ultimate strengths (e.g., [4]). However, the load-deformation characteristics of high strength steel joints can be considerably different from those of mild steel joints, being more flexible and less ductile [5]. With focusing on this aspect, in this study, a re-examination is made for the 3% deformation limit and also for other existing mild steel-based deformation limits available in literature. A modified deformation limit is suggested for CHS joints loaded by in-plane bending (IPB) such that different load-deformation characteristics between mild and high strength steel joints can be accounted for.

In addition, the strain limit newly suggested by Kožich et al. (2019) [6] is also dealt with in this study. The strain limit criterion seems to have the potential to be developed as a practical, mesoscale fracture criterion in relation to the finite element (FE) analysis of tubular joints. For flexible joints, deformation limit criteria such as the 3% rule can be readily utilized to obtain the ultimate capacity from FE analysis results. However, stiff or less ductile joints may be susceptible to fracture at low deformation, and it would be very desirable if a simple fracture criterion could be checked based on somewhat more refined FE analysis. Fig. 1(b) shows an example of an idealized use of strain limit criteria. Consideration of a suitable strain limit seems particularly desirable for high strength steel joints because of their higher susceptibility to cracking.

It should be noted that rigorous fracture criteria may be checked through sophisticated FE analysis by incorporating a material damage model which can describe the crack initiation and propagation explicitly. Unfortunately, the parameters in describing the material damage are known to vary widely among different joint types and should be

* Corresponding author.
E-mail address: ceholee@snu.ac.kr (C.-H. Lee).

https://doi.org/10.1016/j.tws.2022.109681
Received 21 March 2022; Received in revised form 19 May 2022; Accepted 21 June 2022
Available online 6 July 2022

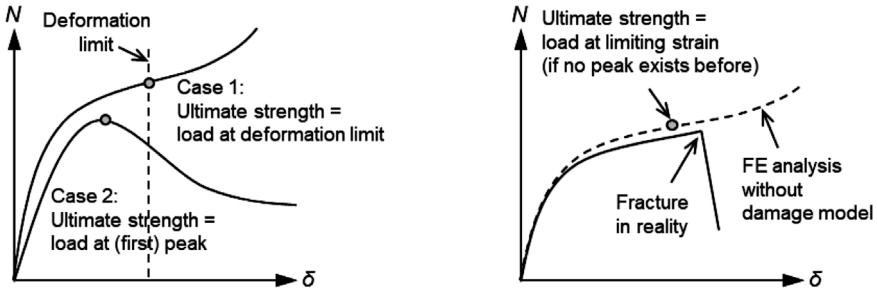

(a) Deformation limit (b) Strain limit

Fig. 1. Determination of ultimate strength based on deformation or strain limit.

calibrated case-by-case with experimental results [7]. Recently, as a practical, design-oriented alternative to the rigorous material damage model, the latest draft of ISO 14346 [8] has advocated the use of a limiting strain in checking the fracture. A principal strain level of 5% was suggested as the limiting strain based on the work of Kožich et al. [6].

In this study, the feasibility of using the 5% strain limit is evaluated for IPB-loaded high strength steel CHS joints. Because clear guidance is not yet available on the size of meshes required for the convergence of the strain in FE analysis, a comprehensive mesh sensitivity study is conducted. Recommendations are made on the FE modeling strategy and step-by-step procedure for the converged strain calculation.

The modifications proposed for the deformation and strain limits are experimentally validated using the available test data. The remainder of the paper is organized as follows. Previous studies on deformation and strain limits are reviewed in Section 2. In Section 3, existing deformation limits are re-examined and a modified deformation limit is presented which is more suited for high-strength steel joints. A modification of the 5% strain limit is suggested in Section 4, and recommendations are also made on the detailed procedures of FE modeling and strain calculation. The summary and conclusions of this study follow in Section 5.

2. Brief review of previous studies

2.1. Deformation limit for IPB-loaded joints

The widely accepted 3% deformation limit was initially suggested by Lu et al. (1994) [3]. This limit was later adopted by the second edition of the CIDECT design guides [1,2]. The 3% deformation limit corresponds to the deformed state of the joint at which maximum deformation on the chord connecting face reaches 3% of the chord diameter (CHS) or width (RHS). With a given deformation limit, the ultimate joint strength is determined as the preceding one between the first peak load and the load corresponding to the deformation limit. The utility of the 3% rule has been confirmed for some types of joint geometry and loading. However, for some joints with other geometries and loadings, different deformation limits were often preferred. According to the authors' literature survey, particularly, for the joints loaded by IPB, three deformation limits were proposed:

(i) Yura et al. (1980) [9]: Yura et al. proposed the maximum permissible joint rotation angle as $(80 f_y/E)$ under IPB.

(ii) Lu and Wardenier (1994) [10]: Since the 3% deformation limit [3] would allow unreasonably large rotation in small brace joints (i.e., small β) subjected to IPB, Lu and Wardenier (1994) suggested an additional rotational limit for I-beam to RHS connections loaded in IPB. This limit corresponds to the chord face rotation angle of 0.1 rad for CHS-to-CHS connections. For the analysis of RHS-to-RHS connections under IPB, Yu (1997) [11] also prescribed a maximum chord face rotation of 0.1 rad in addition to the 3% deformation limit.

(iii) Qian (2005) [12]: Another criterion on the ultimate strength determination was proposed by Qian using a plastic limit load approach. This energy-based criterion defines the limiting deformation as the deformation at the instant when the plastic work done becomes three times the elastic work done. Strictly speaking, Qian's limit belongs to a "plastic energy limit" and may not be referred to as a deformation limit. Nonetheless, in this study, Qian's limit is also regarded as a deformation limit because this limit also aims at preventing excessive inelastic deformation of the joint.

The three deformation limits mentioned above were suggested for mild steel joints. However, the suitability of these limits should further be examined for high-strength steel joints. From the perspective of the plastic rotation capacity of a joint, Yura's limit yields a contradiction in that it permits more deformation to less ductile high-strength steel material. Meanwhile, Lu's limit is neutral to the steel grade. The deformation limit criteria proposed by Lu and Qian will be evaluated including high strength steels in Section 3.

It should be mentioned here that a preliminary evaluation of the deformation limit was tried in a previous study by the authors [13]. However, in the previous study, the joint rotation angle under IPB load was calculated less rigorously using the measured displacement at the tip of the brace member. With the brace tip displacement being used, the joint rotation angle might have been somewhat overestimated, as will be shown later in Fig. 17(b). In this study, the joint deformation and joint rotation angle are more rationally defined for more reasonable proposal of deformation limit.

2.2. Strain limit as an alternative

As previously mentioned in the introduction section (Section 1), the 5% principal strain limit was recently introduced by Kožich et al. (2019) [6] and was adopted in the revised draft of ISO 14346 [8]. The idea of using the limiting strain of 5% for tubular joints originated from Annex C of EN 1993-1-5 [14], wherein the 5% strain limit is recommended for the plated structural elements that are subjected to tensile stresses. The most conservative way of applying the strain limit to a tubular joint is to monitor the principal strains of all elements in the FE model. However, monitoring all elements would not be necessary in most cases if critical locations are obviously known. Near the joint weld, the strain can be highly sensitive to the distance from the weld toe. Kožich et al. [6] recommended that the strain be measured at a stand-off distance of $0.5t$ from the weld toe, where t is the thickness of the tubular member from which the strain is measured.

In the FE study by Kožich et al. [6], the 5% strain limit was evaluated for RHS-to-RHS X joints and branch plate-to-CHS XP or TP joints. It was observed that the ultimate joint strength determined by applying the 5% strain limit was comparable to that determined based

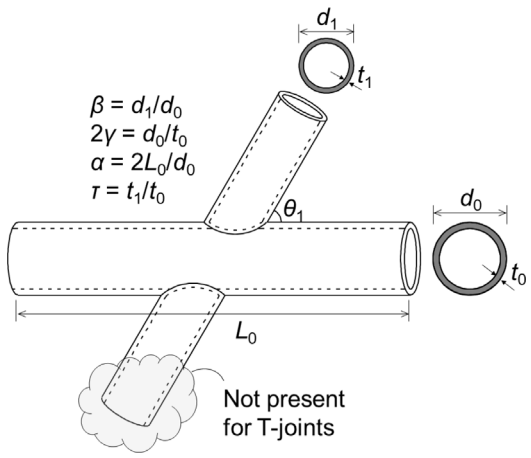

Fig. 2. Geometric configuration of CHS-to-CHS X and T joints.

on the conventional 3% deformation limit criterion, indicating that the 5% strain limit may be adopted as an alternative to the deformation limit for flexible joints that are not susceptible to fracture. However, it appears that the feasibility of the 5% strain limit as a fracture criterion has not been investigated for stiff or less ductile joints in which fracture failure may take place at small deformation.

The size of the (finite) element considered by Kožich et al. [6] was 0.25 times the thickness ($0.25t_0$ for the chord, $0.25t_1$ for the brace), and accurately reproduced the experimental load-deformation relationship. However, the element size required for the accuracy in strain evaluation may be substantially smaller than the typical mesh size used for the determination of the global load-deformation relationship. Therefore, a further mesh sensitivity study seems to be necessary.

Indeed, the concept of the mesoscale strain limit is not new to the tubular joint research. Noting that large tensile strains were observed in CHS K-joints with small gap, Van der Vegte et al. (2002) [15] adopted for mild steel S355 a limiting strain of 20% in their FE analysis as a crack initiation criterion. In their study, cracking was assumed to occur if the strain exceeded 20% at the integration point of the chord element closest to the weld toe. For the analysis of high strength steel joints, a much lower limiting strain would be justified. Dier et al. (2008) [16] also employed a strain limit criterion for CHS X-joints subjected to brace axial tension in determining the crack initiation load from FE analysis. At the weld toe in the saddle region, the plastic strain was measured by an extrapolation technique analogous to that used for the estimation of hot spot stresses. However, the value of limiting strain was not reported.

3. Deformation limit for IPB-loaded high strength steel joints

3.1. FE modeling and analysis

A parametric FE study was conducted on IPB-loaded CHS-to-CHS X- and T-joints for the evaluation of deformation limit using a general-purpose analysis software Abaqus [17]. Material and geometric properties of the FE models are shown in Table 1. The typical geometric configuration of CHS-to-CHS X- and T-joints is presented in Fig. 2 with the definitions of geometric parameters.

One mild (ASTM A500 Grade C [20]) and one high-strength steel (HSA650 [18]) were included as the chord material. The material properties of mild steel were taken from Voth and Packer (2012) [21], and those of the high-strength steel were from the authors' previous tests [19]. Stress–strain curves pertaining to finished cold-formed section were used for the considered steels, which are shown in Fig. 3. The engineering stress–strain curves shown in Fig. 3 were converted to the true stress–strain curves for use in the FE analysis. For the material

Table 1
Material and geometric properties considered for FE analysis.

Property	Values
Steel grade	ASTM A500 Grade C (f_y = 389 MPa, f_u = 527 MPa) HSA650 (f_y = 830 MPa, f_u = 905 MPa)
Joint configuration	X and T ($\theta_1 = 90°$)
d_0	350 mm
β (d_1/d_0)	0.2, 0.47, 0.73, and 1.0
2γ (d_0/t_1)	20, 30, 40, and 50 (50 included only for T joints)
α ($2L_0/d_0$)	20
τ (t_1/t_0)	1.0

[a] HSA650 is a Korean high strength steel whose former name was HSA800. HSA800 was renamed as HSA650 recently, during the revision of the Korean national standard [18]. Although the nominal yield stress is specified as f_{yn} = 650 MPa, the measured mechanical properties of HSA650 are comparable to typical 700 grade steels, e.g., S700 [19].

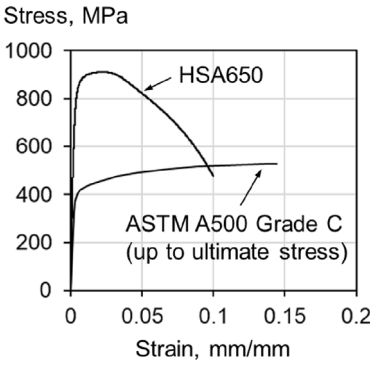

Fig. 3. Stress–strain curves of the mild and high-strength steels investigated.

option, the von Mises yield criterion with isotropic strain hardening was assumed. Material properties of brace and weld were identical to those of the chord.

For the joint geometry, the brace-to-chord diameter ratio β and the chord diameter-to-thickness ratio 2γ were selected within the range of validity specified in prEN 1993-1-8:2021 [22], i.e., $0.2 \le \beta \le 1.0$ and $2\gamma \le 40$ (X-joint) or 50 (T-joint). The selected values were β of 0.2, 0.47, 0.73 and 1.0, and 2γ of 20, 30, 40 and 50 (50 is included only for T-joints). However, the cross-section compactness requirement (Class 1 or 2) was not conformed. This was because, while the selected 2γ ratios (20~50) well represent the common sizes of CHSs available in the market, most of these ratios fall outside the Class 2 limit for high strength steel.

Chord diameter and length were fixed to 350 and 3500 mm, respectively. A chord longer than ten times its diameter is known to have a saturated length from joint strength perspective [4]. For the exclusion of premature brace failure, sufficiently thick members were used for the brace; the brace thickness was identical to the chord thickness in all FE models or the τ ratio was 1.0. Only the orthogonal joints ($\theta_1 = 90°$) were included.

Examples of FE models are presented in Fig. 4. The automatic FE generation code developed by the authors [23] was utilized for the modeling. The 20-node solid element with reduced integration (C3D20R in Abaqus) was used to obtain increased accuracy rather than the computationally less demanding shell element (e.g., S4R) or 8-node solid element (e.g., C3D8R). Three layer meshes were used through the thickness of the chord to accurately capture the chord local bending mechanism. Rotational displacement-controlled moment loading was applied to the brace end. For the T-joints, the ends of the chord member were simply supported. The cross-sections at the ends of chord and brace were modeled as a rigid body, with the reference node located in the center of the cross-section.

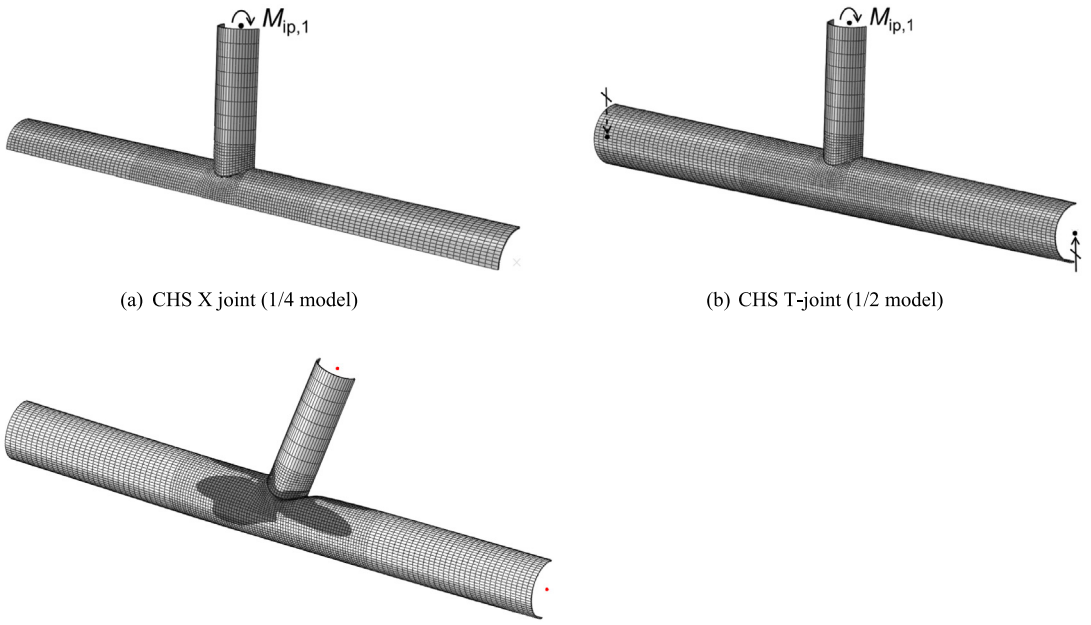

(a) CHS X joint (1/4 model)

(b) CHS T-joint (1/2 model)

(c) Example of joint yield pattern (T-joint, dark region indicates yielding)

Fig. 4. FE models for IPB-loaded CHS X and T joints.

Table 2
Data screening for exclusion of chord punching shear.

X-joints (O = valid, X = screened)				
	$2\gamma = 20$	$2\gamma = 30$	$2\gamma = 40$	
$\beta = 0.20$	X	X	O	
$\beta = 0.47$	X	O	O	
$\beta = 0.73$	X	O	O	
$\beta = 1.0$	X	O	O	
T-joints (O = valid, X = screened)				
	$2\gamma = 20$	$2\gamma = 30$	$2\gamma = 40$	$2\gamma = 50$
$\beta = 0.20$	X	X	O	O
$\beta = 0.47$	X	O	O	O
$\beta = 0.73$	X	O	O	O
$\beta = 1.0$	X	X	O	O

The validation of the FE modeling is not presented in this section but relevant discussions can be found later in Section 4.1. The FE analysis results of IPB-loaded CHS joints were shown to be greatly influenced by small changes in the weld size and profile. In Section 4.1, a comprehensive comparison is made between the experimental data and FE simulation results considering the high sensitivity with respect to the weld geometry (Figs. 26 and 31).

Because consideration for the chord punching shear was not made in the FE analysis, the geometries related to the punching shear behavior were excluded by properly screening the data. If the maximum joint load until 0.1 rad joint rotation exceeded 1.25 times the punching shear design resistance of prEN 1993-1-8 [22], the FE model was regarded as invalid and was screened out. The screened results are shown in Table 2.

3.2. Evaluation of existing deformation limits and a new proposal

In Section 2.1, three deformation limits for IPB-loaded tubular joints were introduced: Yura, Lu, and Qian's limit. Yura's limit is contradictory when both mild and high strength steels are taken into account. Remaining two limits are discussed in this section based on FE analysis results.

Fig. 5 presents the evaluation made on Qian's energy-based criterion. The joint rotation angle was calculated from the deformations at the crown points (see Fig. 6). The crown point deformations (δ_A, δ_B) were obtained by deducting global member deflection component from the total displacement at the crown point.

$$\delta_A = u_A - u_{A'}, \delta_B = u_B - u_{B'} \tag{1}$$

where u represents the displacement in the brace axis direction (i.e., the direction perpendicular to the chord connecting face). It was assumed that the global deflection of the chord member can be represented by the deflection along the mid-sidewall. With δ_A and δ_B, the joint rotation (φ) can be obtained as follows.

$$\varphi = \frac{\delta_A - \delta_B}{\overline{AB}} \tag{2}$$

where the distance between A and B is equal to the distance between the weld toes (slightly larger than the brace diameter).

In Fig. 5, plastic rotation was obtained by excluding any elastic component through unloading; i.e., the points marked on the x-axis represent the plastic rotation permitted. It is clearly seen that smaller plastic rotation is permitted for more ductile mild steel joints (ASTM A500 Grade C; denoted as "A500 C") with Qian's criterion. It should be noted that "effective yielding" (or significant loss of stiffness) occurs at considerably larger rotation in high-strength steel joints, and this seems to be the main reason for the contradictory trend of permitted plastic rotation. It is not suitable to adopt Qian's criterion for IPB loading when a wide range of steel grades is involved.

Fig. 7 shows the normalized moment versus rotation relationship of CHS X and T-joints. The y-axis in Fig. 7 corresponds to the IPB moment normalized by $f_{y0}t_0^2 d_1 \beta\gamma^{0.5}$ [24]. A peak load mostly exists in the moment–rotation diagrams of joints with larger β ratios ($\beta = 0.73$ and 1.0) while monotonically increasing curves are shown for joints with smaller β ratios ($\beta = 0.2$ and 0.47). The open circles in Fig. 7 represent the deformation limit according to Lu's criterion, which is the lesser of the $3\%d_0$ deformation ($\delta = 3\%d_0$) and the joint rotation angle of 0.1 rad ($\varphi = 0.1$ rad). Except for the small-braced joints with $\beta = 0.2$, $\delta = 3\%d_0$ mostly precedes $\varphi = 0.1$ rad such that the Lu's deformation limit is governed by $\delta = 3\%d_0$.

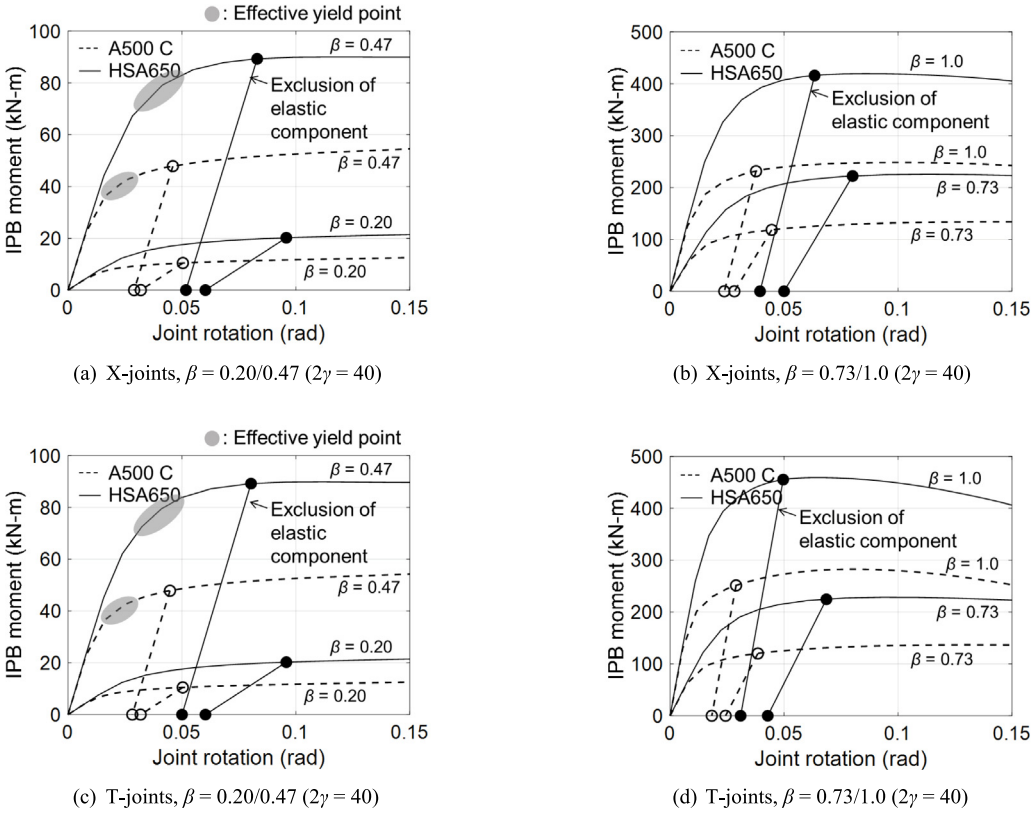

(a) X-joints, $\beta = 0.20/0.47$ ($2\gamma = 40$)

(b) X-joints, $\beta = 0.73/1.0$ ($2\gamma = 40$)

(c) T-joints, $\beta = 0.20/0.47$ ($2\gamma = 40$)

(d) T-joints, $\beta = 0.73/1.0$ ($2\gamma = 40$)

Fig. 5. Evaluation of Qian's energy-based criterion.

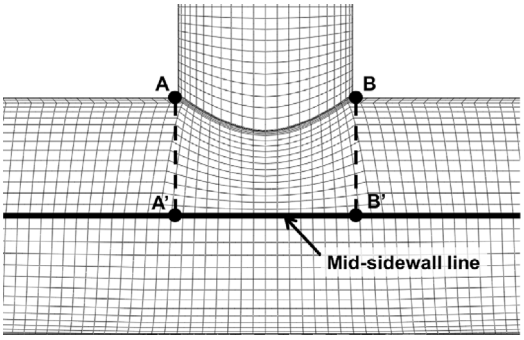

Fig. 6. Displacement-measuring locations to obtain joint rotation angle.

The deformation capacity of the IPB-loaded joints may be evaluated with the method introduced by Lee et al. (2017) [4], which is shown in Fig. 8(a). According to Lee et al. [4], for axially loaded joints, the ultimate deformation (δ_u) and effective yielding deformation (δ_y) are defined by the two intersecting points between the load-deformation diagram and an equivalent bilinear curve with the same internal work done. The ultimate deformation (δ_u) or the ratio of ultimate deformation to the yielding deformation (i.e., δ_u/δ_y) may be regarded as an index for the joint deformation capacity. In Fig. 8(b), the equivalent bilinear curves are drawn for the IPB-loaded joints of this study. Only the joints with $\beta = 1.0$ and $2\gamma = 50$ (Fig. 7(h)) are presented because the ultimate rotation angle (φ_u) was the smallest with these geometric parameters. It appears that the lower ductility of high strength steel joints is well represented by the decrease in the ultimate rotation angle (φ_u).

Considering that the reduced ductility capacity of IPB-loaded high strength steel joints is primarily related to the low strain hardening property of high strength steel, a new deformation limit for IPB loaded joints in terms of joint rotation angle may be suggested based on the ultimate-to-yield stress ratio (f_{u0}/f_{y0}) as follows.

$$\varphi_{lim} = \frac{1}{15}\left(\frac{f_{u0}}{f_{y0}}\right) \text{(rad)} \tag{3}$$

The idea behind Eq. (3) is that the maximum permitted joint rotation angle should be proportional to f_{u0}/f_{y0}. By setting the deformation limit of S235 equal to the joint rotation angle of 0.1 rad, the following formulation can be derived.

$$\varphi_{lim} = 0.1 \times \left(\frac{f_{u0}}{f_{y0}}\right) \Big/ \left(\frac{f_u}{f_y}\right)_{S235} = \frac{0.1}{1.53}\left(\frac{f_{u0}}{f_{y0}}\right) \approx \frac{1}{15}\left(\frac{f_{u0}}{f_{y0}}\right) \text{(rad)} \tag{4}$$

In Fig. 8(b), the proposed rotation angle limit is compared with the ultimate rotation angle φ_u. The proposed limit (φ_{lim}) seems to provide a reasonable correlation to the decrease in φ_u with the use of high strength steel. The proposed deformation limit is also marked in Fig. 7.

The idea of the strain-hardening-based limit of Eq. (3) was also introduced in the preliminary study by the authors [13], and this idea was further extended to longitudinal branch plate-to-CHS XP and TP joints by Han et al. (2021) [25]. The typical geometric configuration of longitudinal branch plate-to-CHS XP and TP joints is presented in Fig. 9 with the definitions of geometric parameters. Han et al. [25] found that applying the conventional 3% rule results in too severe underrating of strength for IPB-loaded longitudinal plate-to-CHS joints with high η ratios ($\eta > 1.0$).

As shown in Fig. 10, the 3% deformation criterion limits the joint load to a loading stage where inelastic behavior has been limited. For more reasonable rating of IPB strength of the plate connections with high η, the authors extended Eq. (3) and recommended a more generalized rotation angle limit which is applicable to both CHS-to-CHS and plate-to-CHS connections as follows.

$$\varphi_{lim} = \frac{1}{15 \cdot (\eta \text{ or} \beta)} \frac{f_{u0}}{f_{y0}} \le \frac{1}{15}\frac{f_{u0}}{f_{y0}} \text{ rad} \tag{5}$$

(η for branch plate, β for CHS brace)

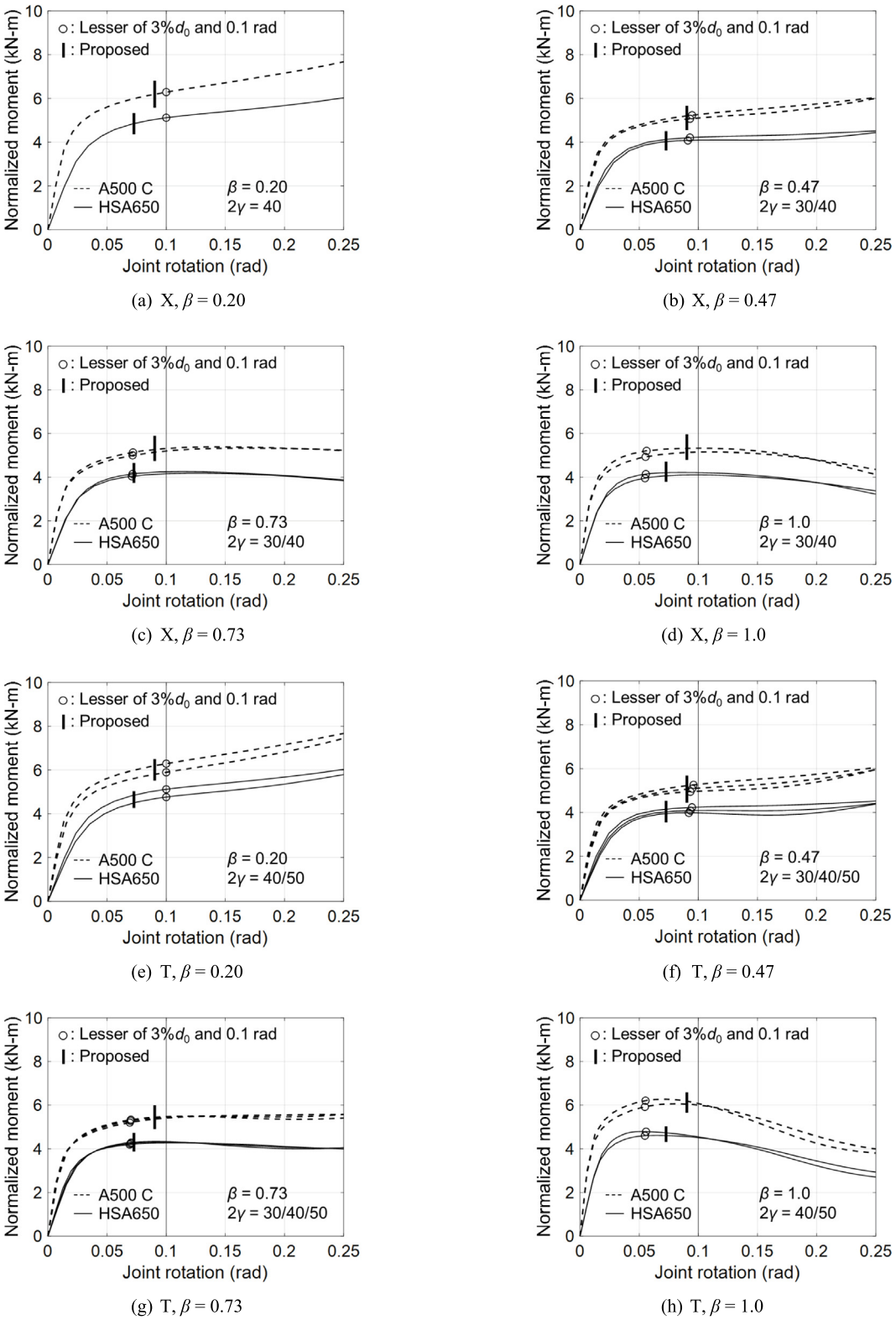

(a) X, $\beta = 0.20$ (b) X, $\beta = 0.47$

(c) X, $\beta = 0.73$ (d) X, $\beta = 1.0$

(e) T, $\beta = 0.20$ (f) T, $\beta = 0.47$

(g) T, $\beta = 0.73$ (h) T, $\beta = 1.0$

Fig. 7. Evaluation of Lu's criterion and new deformation limit proposed.

The rotation angle limit suggested for IPB loading can be utilized also for joints subjected to combined axial and IPB loading [25]. When both axial load and IPB moment are present, it is recommended to apply two deformation limits simultaneously, one to joint indentation component and the other to joint rotation component. As shown in Fig. 11, the local joint deformation under the combined loading can be divided into the average indentation component δ_{avg} (Eq. (6)) and the rotation component φ (Eq. (7)). The ultimate joint deformation is assumed to have reached when either δ_{avg} reaches $0.03d_0$ or φ reaches φ_{lim} (Eq. (5)), whichever is earlier. Please note that the original 3% limit corresponds to δ_1 or δ_2 (whichever is larger) = $0.03d_0$, not δ_{avg} = $0.03d_0$. Thus, the proposed limit on the average indentation component

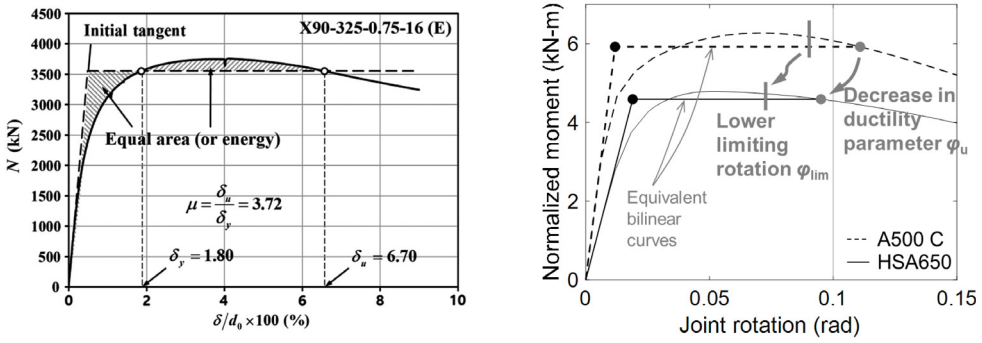

(a) Equivalent bilinear curve and definition of ultimate deformation [4]

(b) Ultimate joint rotations of T-joints with $\beta = 1.0$ and $2\gamma = 50$ (Fig. 7(h))

Fig. 8. Rationale behind proposed joint rotation angle limit.

Table 3
Material and geometric properties of test specimens.

ID	Material properties			Geometric properties						Non-dimensional parameters		
	Steel grade	f_{y0} (MPa)	f_{u0} (MPa)	d_0 (mm)	t_0 (mm)	h_1 or d_1 (mm)	t_1 (mm)	L_0 (mm)	l_1 (mm)	η or β[d]	2γ	α
C-XP2-I-460	SM460[a]	609.0	672.1	249.5	9.4	249.0	30.0	1500[c]	1100	1.0	27	12
C-X-I-700	ATOS80[b]	761.5	834.2	299.0	10.1	249.4	10.1	1498	1106	0.83	30	10

[a]Nominal properties of SM460: $f_{yn} = 460$ MPa, $f_{un} = 570$ MPa.
[b]Nominal properties of ATOS80: $f_{yn} = 700$ MPa, $f_{un} = 780$ MPa.
[c]Nominal value used (not measured).
[d]η for plate-to-CHS joints (C-XP2-I-460) and β for CHS-to-CHS joints (C-X-I-700).

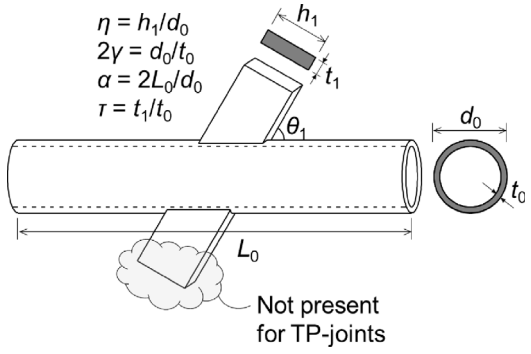

Fig. 9. Geometric configuration of longitudinal plate-to-CHS XP and TP joints.

(δ_{avg}) is the same with the original 3% limit only when pure axial loading is applied or $\varphi = 0$.

$$\delta_{avg} = \frac{\delta_1 + \delta_2}{2} \tag{6}$$

$$\varphi = \frac{\delta_1 - \delta_2}{h_1} \tag{7}$$

Fig. 12 shows an example for the determination of ultimate strength under combined loading. In this example, the peak IPB moment develops before reaching the joint rotation limit ($\varphi_{lim} = 0.023$ rad according to Eq. (5), with $f_{y0} = 356$ MPa, $f_{u0} = 497$ MPa, and $\eta = 4.0$). However, the ultimate IPB strength is determined even before the peak because the state corresponding to the axial indentation limit ($\delta_{avg} = 0.03d_0$) comes earlier (Fig. 12(b)). Thus, the combined joint strength is determined as N_{uc} and M_{uc} as marked in Fig. 12.

The simultaneous application of average indentation limit and rotation angle limit may be better understood with Fig. 13, which shows the evolution of the joint deformation depending on the ratio of axial-to-IPB loading [25]. The three solid lines correspond to the combined loading cases with different ratios between axial compression and IPB moment. Based on the ultimate resistances under pure axial force (N_u) and pure IPB moment (M_u), the ratios between applied axial force and IPB moment were set proportional to $0.75N_u$:$0.25M_u$, $0.50N_u$:$0.50M_u$, or $0.25N_u$:$0.75M_u$ for the three combined loading cases. The circles represent the state corresponding to the ultimate joint deformation according to the proposed criterion. As expected, the joint rotation component becomes more critical as the portion of the bending moment increases. It is noteworthy that slight joint indentation occurs even under pure IPB loading. This non-symmetric local deformation is due to the higher stiffness at the tension side of the IPB joint compared to the compression side.

3.3. Experimental validation of proposed limit

For experimental validation of the proposed criterion, two CHS joints were tested. Fig. 14 shows the setup for the joint specimens tested. One branch plate-to-CHS XP-joint (C-XP2-I-460, Fig. 14(a)) and one CHS-to-CHS X-joint (C-X-I-700, Fig. 14(b)) were tested under IPB loading.

For each specimen, the ends of the two branch members were supported with rollers, and downward loading was applied to the chord end to produce IPB moment on both sides of the joint. The downward displacement was measured with two linear variable differential transformers (LVDTs). As shown in Fig. 14(c–d), stiffeners were provided at the ends of the branch members to prevent local deformation near the roller support. For the plate-to-CHS XP-joint specimen C-XP2-I-460, premature out-of-plane buckling of the branch plate was prevented through the top flange reinforcement.

Material and geometric properties of the tested joints are shown in Table 3. A 460-grade steel SM460 was used for C-XP2-I-460 and a 700-grade steel ATOS80 was used for C-X-I-700. Because the tubular members were cold formed, the yield and ultimate stresses obtained from curved coupons are reported in Table 3; these values were used in calculating the deformation limit (Eq. (5)) or design resistance.

Fig. 15 shows the deformed shapes and failure modes of the joints after testing. C-XP2-I-460 failed finally by punching shear, while weld

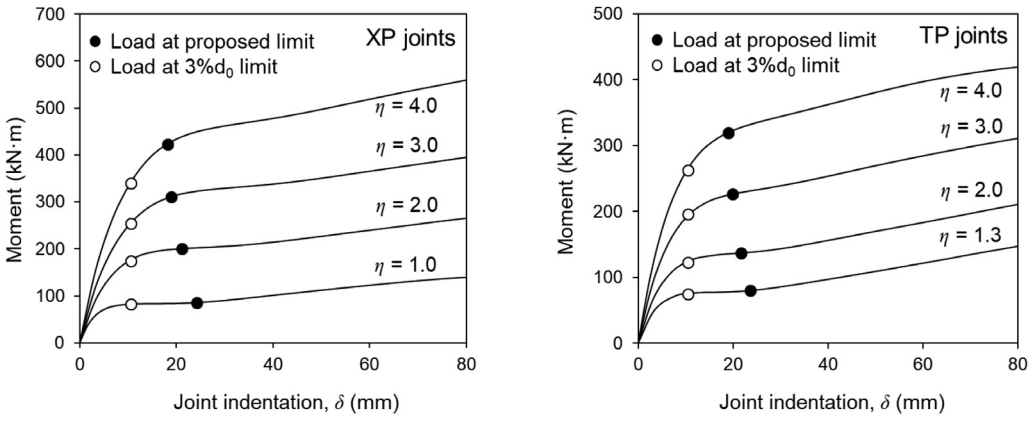

(a) XP joints (b) TP joints

Fig. 10. Extension of proposed rotation angle limit to longitudinal plate-to-CHS joints [25].

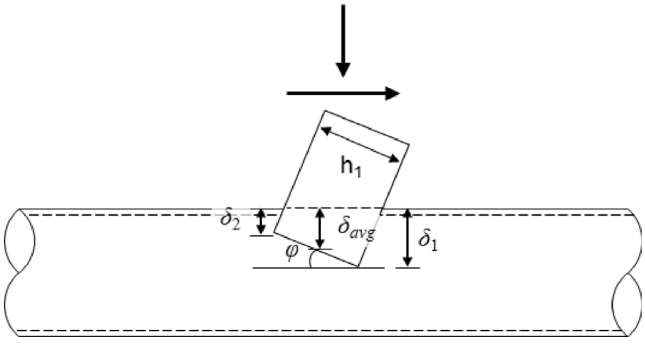

Fig. 11. Average joint indentation and joint rotation angle.

cracking near the weld toe was observed in C-X-I-700. Fig. 16 presents the IPB moment versus joint rotation relationship of the two tested joints. Because IPB moment and joint rotation angle were not directly measured during testing, as shown in Fig. 17, these values were calculated from the measured downward force (N) and downward displacement (Δ).

First, the IPB moment was calculated by multiplying the reaction force at the support (0.5 N) with the arm length l_1 (Fig. 17(a)). To derive the joint rotation angle (Fig. 17(b)), the displacement component produced by the deflection of the branch member (Δ_{def}) was deducted from the measured displacement to obtain the pure joint rotation component ($\Delta_{rot} = \Delta - \Delta_{def}$). Δ_{def} was calculated with assuming the branch member as an elastic Bernoulli (shallow) beam subjected to the cantilever load of 0.5 N. After extracting the pure joint rotation component out of the total displacement, the joint rotation angle can be obtained by $\varphi = \Delta_{rot}/l_1$. The solid line in Fig. 16 indicates the moment–rotation curves that were drawn according to the procedure described in Fig. 17.

Alternatively, one may calculate the joint rotation angle in a more practical manner, by $\varphi = \Delta/l_1$, without excluding the displacement component caused by the branch deflection. Moment–rotation curves based on the "branch deflection-included" joint rotation angle are also presented in Fig. 16 with dotted lines. In Fig. 16, marginal difference is shown between the rigorous moment–rotation curve (solid line) and the practical moment rotation curve (dotted line).

The ultimate joint strength was determined as the peak load for XP2-I-460 (Fig. 16(a)) and as the load at the rotation angle limit (Eq. (5)) for C-X-I-700 (Fig. 16(b)). For both specimens, the rotation angle limit was placed well before the cracking. To further investigate the utility of the rotation angle limit as a fracture criterion for IPB loaded joints, more experimental moment–rotation curves were collected from available test database as shown in Fig. 18.

Only high-strength steel data were included in Fig. 18 since fracture failures due to IPB loading are rarely expected in mild steel joints until excessive rotation. Grade 460 steels were considered for plate-to-CHS joints (XP and TP joints) and grade 700 steels were considered for CHS-to-CHS joints (X and T joints). Moment–rotation curves are presented for six XP-joints in Fig. 18(a–b) [26], two X-joints in Fig. 18(c) [27], and one T-joint in Fig. 18(d) [28]. For TP-joints, no relevant test data was available.

In Fig. 18(a–b), although the onset of fracture was not reported for these XP-joints, the rotation angle limit is located near the peak load or the plateau on the moment–rotation relationship. It is more clearly shown in Fig. 18(c–d) that the rotation angle limit well captures the nonlinear load-bearing capacity of the IPB joints before the occurrence of the fracture failures. Overall, in both Figs. 16 and 18, the rotation angle limit appears to give an appropriate evaluation of the ultimate resistance.

The practical moment–rotation curves based on branch deflection-included joint rotation angle are also presented in Fig. 18 (dotted line). Particularly, in Fig. 18(c), a notable difference is seen between the rigorous (solid line) and practical (dotted line) moment–rotation curves. For such cases, ultimate joint resistance would be somewhat underestimated if the practical moment–rotation curve is used.

3.4. Design resistance of high strength steel CHS joints

Based on the joint rotation angle limit proposed in the above section, the design resistance of high-strength steel CHS-to-CHS joints is discussed below. According to the prEN 1993-1-8 [22], for CHS-to-CHS X and T joints, the axial and IPB design resistances which are based on the reanalysis by Van der Vegte (2008) [29] are given for chord plastification (chord failure) by the following limit states.

$$N_{1,Rd} = C_f \frac{f_{y0} t_0^2}{\sin\theta_1}\left(\frac{2.6 + 2.6\beta}{1 - 0.7\beta}\right)\gamma^{0.15} Q_f/\gamma_{M5}$$

(for axially loaded CHS X joints) (8)

$$N_{1,Rd} = C_f \frac{f_{y0} t_0^2}{\sin\theta_1}(2.6 + 17.7\beta^2)\gamma^{0.2} Q_f/\gamma_{M5}$$

(for axially loaded CHS T joints) (9)

$$M_{ip,1,Rd} = 4.3 C_f \frac{f_{y0} t_0^2 d_1}{\sin\theta_1}\beta\gamma^{0.5} Q_f/\gamma_{M5}$$

(for IPB-loaded CHS X and T joints) (10)

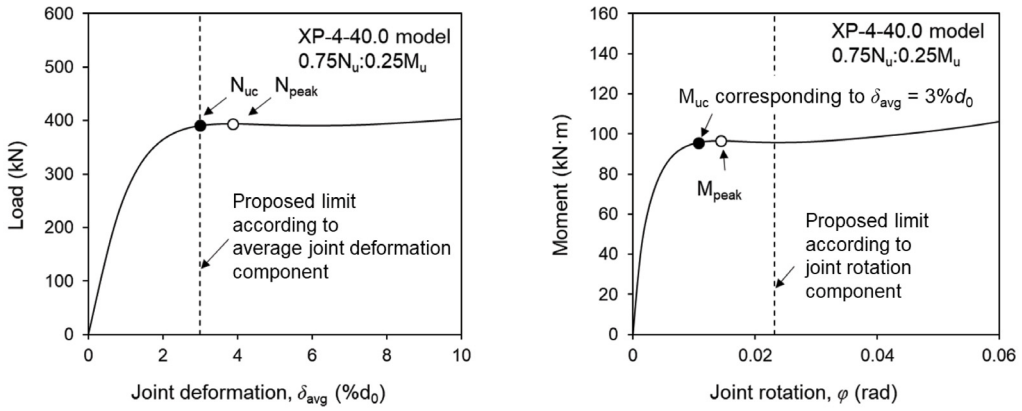

(a) Axial force-average indentation curve (b) IPB moment-rotation curve

Fig. 12. An illustration of determination of ultimate strength under combined axial force and IPB moment [25].

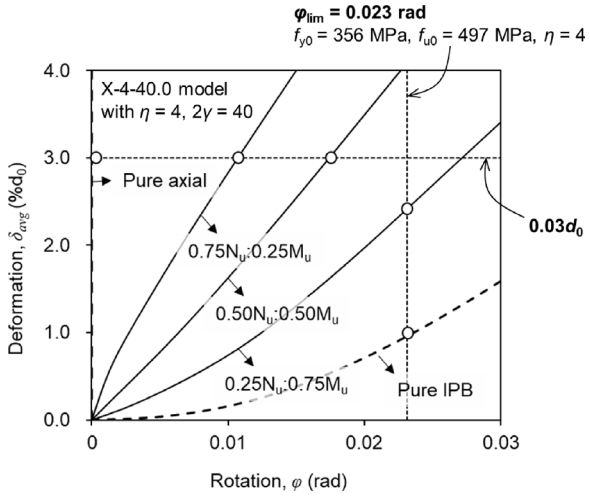

Fig. 13. Evolution of deformation in XP joints under combined loading [25].

The design resistances in Eqs. (8)–(10) consist of the basic design equation applicable to mild steel joints and a material factor C_f accounting for the relatively lower resistance based on the yield stress of high strength steel joints. The material factor C_f is, according to prEN 1993-1-8, 0.9 for S460 and 0.8 for S700.

For CHS-to-CHS joints loaded by combined axial force and IPB, prEN 1993-1-8 provides a design interaction relation as Eq. (11). The parabolic (convex-upward) interaction equation of Eq. (11) is rooted in the experimental observation on CHS X-joints made by Hoadley and Yura (1985) [30]. Marshall (1984) [31] found that the failure envelope for CHS T-joints is also more optimistic than the linear envelope. prEN 1993-1-8 recommends the same parabolic curve adopted for X-joints (Eq. (11)) to be used for T-joints as well. Because only mild steels were considered in the experimental studies by Hoadley and Yura (f_{ym} = 321~331 MPa) [30] and Marshall (f_{ym} = 320~388 MPa) [31], additional check is required for the interaction behavior of high-strength steel joints.

$$\frac{|N_{1,Ed}|}{N_{1,Rd}} + \left(\frac{M_{ip,1,Ed}}{M_{ip,1,Rd}}\right)^2 \le 1.0 \tag{11}$$

In this section, the applicability of the material factor and design interaction equation specified in prEN 1993-1-8 are evaluated for high strength steel CHS-to-CHS joints. For longitudinal plate-to-CHS joints made of high strength steel, the related discussions can be found in Han et al. (2021) [25].

Finite element (FE) analysis was performed on the chord plastification behavior of CHS X and T joints subjected to combined axial force and IPB. Material and geometric properties considered for the FE models were the same as those shown in Table 1. One mild (ASTM A500 Grade C [20]) and one high-strength steel (HSA650 [18]) were included as the material for the chord (see Fig. 3).

For the combined loading, four different loading ratios between axial compression and IPB were included for each joint geometry; one pure axial compression, one pure IPB moment, and two combined loadings with different loading ratios. The combined loading ratios were determined based on the mean strength equations proposed by van der Vegte et al. [24,29], Eqs. (12)–(15). Based on the mean axial and IPB strengths ($N_{1,m}$ and $M_{ip,1,m}$), the two combined loading ratios were chosen to be $N_{1,m}\cos(30°):M_{ip,1,m}\sin(30°)$ and $N_{1,m}\cos(60°):M_{ip,1,m}\sin(60°)$. Therefore, each joint was analyzed with four different loading ratios, $N_{1,m}\cos\psi:M_{ip,1,m}\sin\psi$ with ψ =0, 30, 60, 90°. Force-controlled loading was applied to the brace end to maintain the load ratio.

$$N_{1,m} = \frac{f_{y0}t_0^2}{\sin\theta_1}\left(\frac{3.16+3.16\beta}{1-0.7\beta}\right)\gamma^{0.15}$$

(for axially loaded CHS X joints) (12)

$$N_{1,m} = \frac{f_{y0}t_0^2}{\sin\theta_1}(3.1+21\beta^2)\gamma^{0.2}$$

(for axially loaded CHS T joints) (13)

$$M_{ip,1,m} = 5.33\frac{f_{y0}t_0^2 d_1}{\sin\theta_1}\beta\gamma^{0.5}$$

(for IPB-loaded CHS X joints) (14)

$$M_{ip,1,m} = 5.69\frac{f_{y0}t_0^2 d_1}{\sin\theta_1}\beta\gamma^{0.5}$$

(for IPB-loaded CHS T joints) (15)

For the FE analysis of T-joints, moment compensation was applied to minimize the effect of chord internal moment on the joint behavior (or to minimize the chord stress effect). The concept of moment compensation is illustrated in Fig. 19.

Bending moment diagrams (BMDs) of the chord member corresponding to axial force N_1 and IPB moment $M_{ip,1}$ are separately shown. While the internal moment induced by axial force can be compensated by properly applying end moments (M_c), it is not possible to completely

(a) C-XP2-I-460

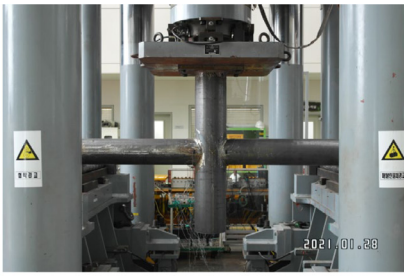

(b) C-X-I-700

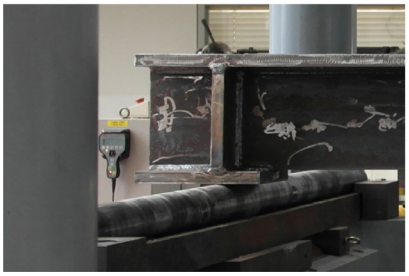

(c) End stiffener detail of C-XP2-I-460

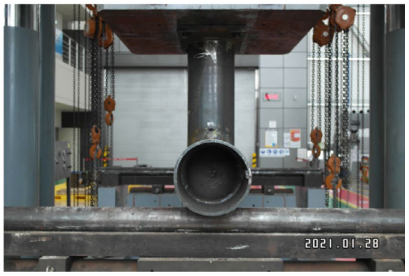

(d) End stiffener detail of C-X-I-700

Fig. 14. Test setup.

(a) Deformed shape of C-XP2-I-460

(b) Punching shear observed in C-XP2-I-460

(c) Deformed shape of C-X-I-700

(d) Weld cracking observed in C-X-I-700

Fig. 15. Deformed shapes and failure modes observed.

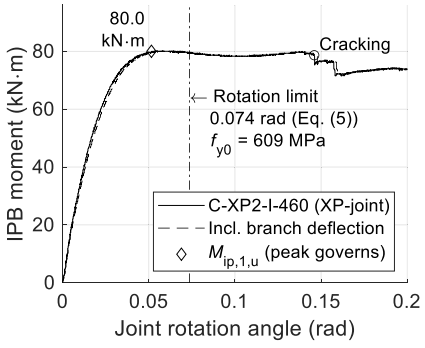

(a) C-XP2-I-460

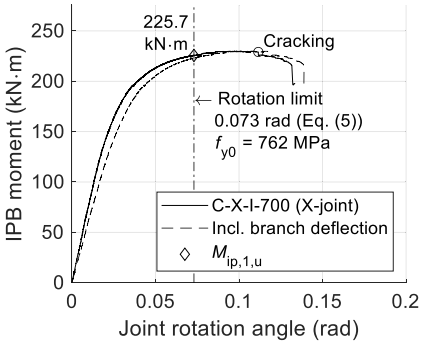

(b) C-X-I-700

Fig. 16. IPB moment versus joint rotation angle relationship.

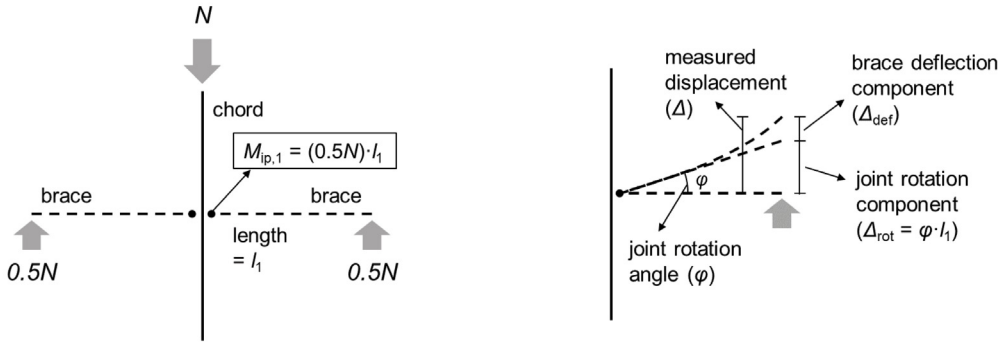

(a) IPB moment (b) Joint rotation angle

Fig. 17. Derivation of IPB moment and joint rotation angle from measured load and displacement.

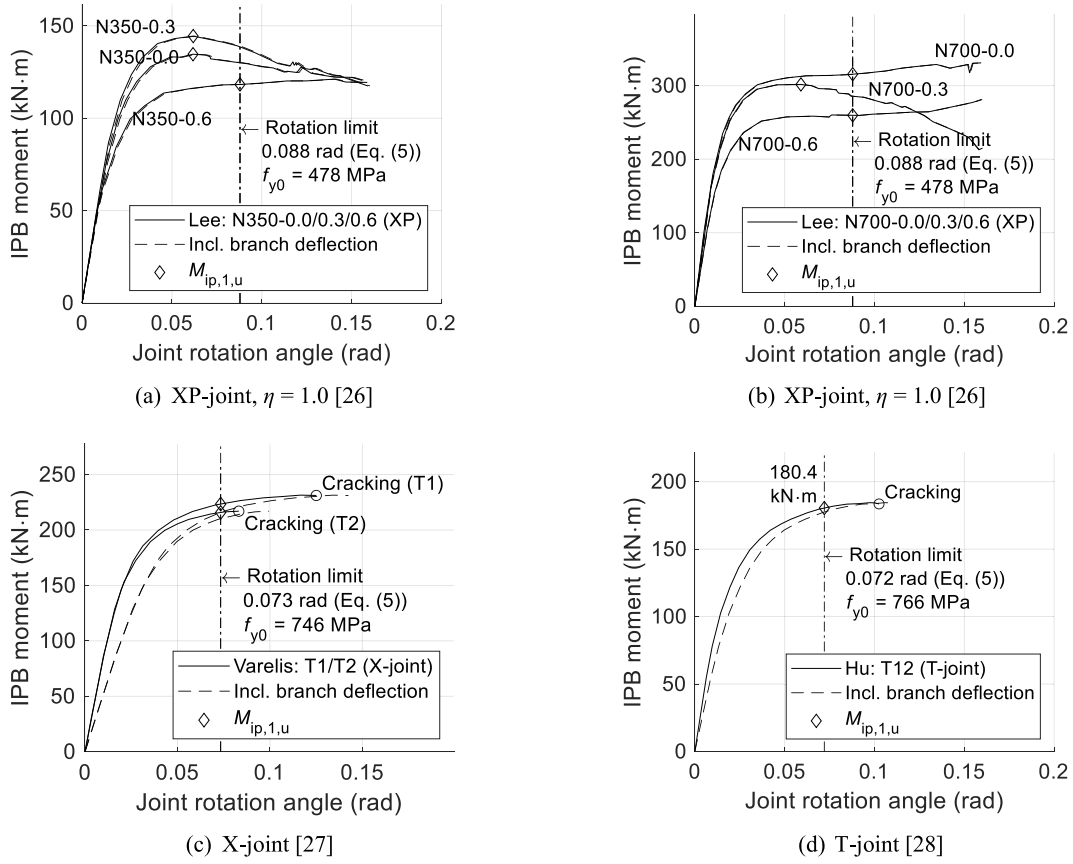

(a) XP-joint, η = 1.0 [26] (b) XP-joint, η = 1.0 [26]

(c) X-joint [27] (d) T-joint [28]

Fig. 18. Evaluation of joint rotation angle limit using available test database.

compensate the internal moment induced by IPB moment. Thus, the moment compensation was applied only to the axial force component of the combined joint loading. The magnitude of M_c increases with increasing N_1 as follows.

$$M_c = \frac{N_1(L_0 - d_1)}{4} \tag{16}$$

where L_0 and d_1 represent the chord length and brace diameter, respectively.

With the compensating end moment, the end part of the chord member has to be strengthened because of the large internal bending moment induced near the chord ends. The length of strengthened region (L_{end}) was determined such that the internal moment in the remaining region ($0.5L_0$-L_{end}) would not exceed the plastic moment capacity (M_p) until the axial force on the joint reaches the mean strength $N_{1,m}$ (Eqs. (12)–(13)). The expression for L_{end} is as follows.

$$0.5N_{1,m} \times [0.5(L_0 - d_1) - L_{end}] = M_p = f_{y0}\frac{{d_0}^3 - (d_0 - 2t_0)^3}{6} \tag{17}$$

$$\therefore L_{end} = 0.5(L_0 - d_1) - f_{y0}\frac{{d_0}^3 - (d_0 - 2t_0)^3}{3N_{1,m}} \geq 0 \tag{18}$$

Although Class 3 and 4 chord cross-sections were included in the FE analysis, L_{end} was calculated based on M_p also for these non-compact sections to avoid unnecessarily lengthy strengthened region. For the strengthened region, the yield stress of the material was increased as

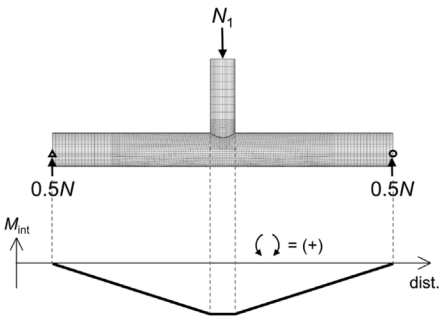

(a) BMD for axial force before compensation

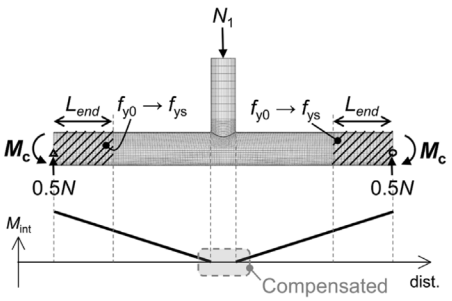

(b) BMD for axial force after compensation

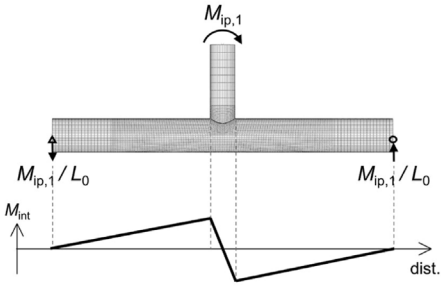

(c) BMD for IPB moment (compensation not applied)

Fig. 19. Moment compensation for CHS T-joints.

follows.

$$\frac{f_{ys}}{f_{y0}} = 1.1\frac{M_c|_{N_1=N_{1,m}}}{M_p} = \frac{1.1N_{1,m}(L_0-d_1)/4}{f_{y0}\left[{d_0}^3-(d_0-2t_0)^3\right]/6} \tag{19}$$

$$\therefore \frac{f_{ys}}{f_{y0}} = \frac{1.65(L_0-d_1)(3.1+21\beta^2)\gamma^{0.2}}{{d_0}^3-(d_0-2t_0)^3} \geq 1.0 \tag{20}$$

where f_{ys} represents the yield stress over the strengthened length and f_{y0} is the original chord yield stress. f_{ys} needs not be taken less than f_{y0}.

Because the FE analysis focused on chord plastification behavior, the FE results were properly screened to exclude chord punching shear. Since CHS joints are more susceptible to chord punching shear under IPB moment compared to axial compression [25], the same screening criterion used in Section 3.1 for IPB loaded joints was also adopted herein (see Table 2).

From the FE analysis results, the ultimate strengths of the joints were determined according to the deformation limit criterion proposed in this paper (see Section 3.2). According to the proposed criterion, for CHS-to-CHS joints subjected to combined axial force and IPB, the ultimate deformed state of the joint is assumed to be reached when either the average joint deformation reaches 3% of the chord diameter or the joint rotation angle reaches φ_{lim} which is defined in Eq. (5). The ultimate joint strength is determined as the load at the ultimate deformed state if there is no peak load until then. If the peak load occurs before reaching the ultimate deformed state, the load at the first peak should be the ultimate strength (refer to Section 3.2 for more details).

The interaction behavior of CHS X and T-joints identified from FE analysis is shown in Figs. 20 and 21. In preparing Fig. 20, the interaction failure envelopes were plotted based on ultimate strength of individual loading case. That is, each axis was normalized by the ultimate strength under pure axial force or pure IPB moment obtained from the FE analysis (therefore, the data points corresponding to the individual loading cases are all placed in either (1,0) or (0,1)). It is noteworthy in Fig. 20 that failure envelope becomes more favorable with increasing β. This tendency may be explained as follows. When β is high, the axial strength of the joint relies more on the saddle region, while the IPB strength of the joint depends more on the crown region. Therefore, less interaction between the two failure modes is expected with higher β. Although the average trend of the data points agrees well with the prEN 1993-1-8 interaction curve (Eq. (11)), the actual failure envelope becomes closer to the linear curve with $\beta = 0.2$. Slight difference is observed between CHS X and T joints and between mild and high strength steel joints. The failure envelope is slightly more favorable for high strength steel joints than for mild steel joints, indicating that the design interaction curve developed for mild steel joints can be conservatively extended to high strength steel joints.

Fig. 21 shows the interaction diagrams plotted based on the normalization with respect to the design resistance according to prEN 1993-1-8. The material factor 0.8 was included in calculating the design resistance of high strength steel joints. Chord stress effect was not considered or the chord stress function Q_f was taken as 1.0 which could have a larger effect for joints with low β ratios. The design resistance gives conservative results for all joints but less safety margin is provided to high strength steel joints. Less margin to high strength steel joints is primarily due to the less conservatism for pure axial loading case (data points on the x-axis). Nonetheless, both the parabolic interaction curve and the material factor of 0.8 specified in prEN 1993-1-8 seem to be acceptable for high strength steel joints.

Please note that the FE analysis of this section only considered the chord plastification failure (chord failure). Further investigation is required for the case of chord punching shear because the interaction behavior may be different when failure mode changes.

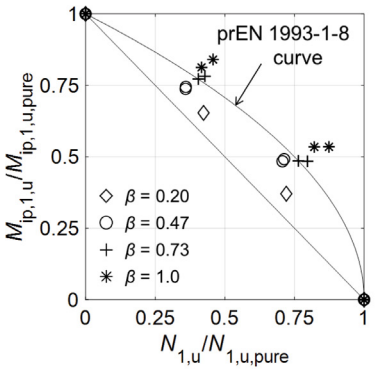

(a) X-joints, mild steel

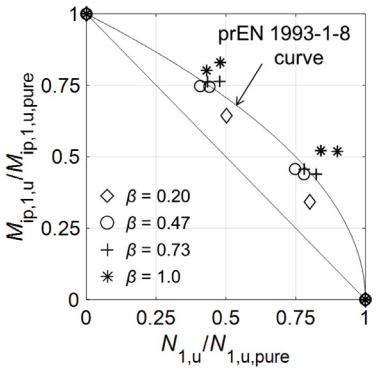

(b) X-joints, high strength steel

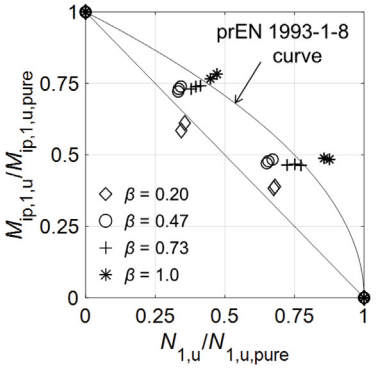

(c) T-joints, mild steel

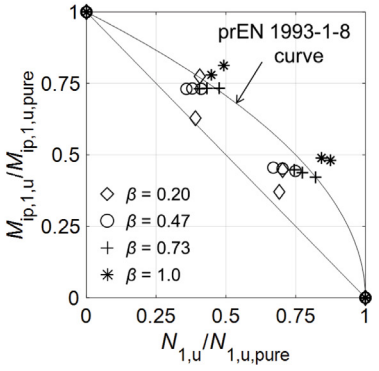

(d) T-joints, high strength steel

Fig. 20. IPB-axial force interactive envelope based on normalization with respect to ultimate resistance of individual loading.

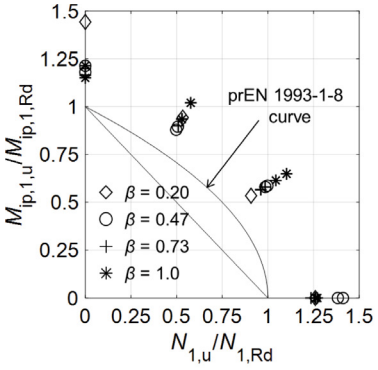

(a) X-joints, mild steel

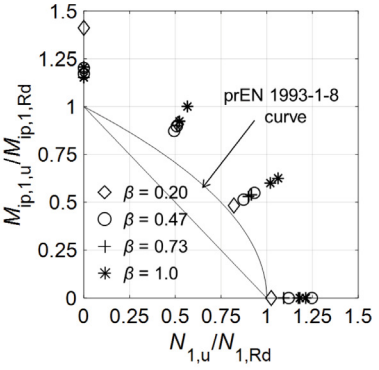

(b) X-joints, high strength steel

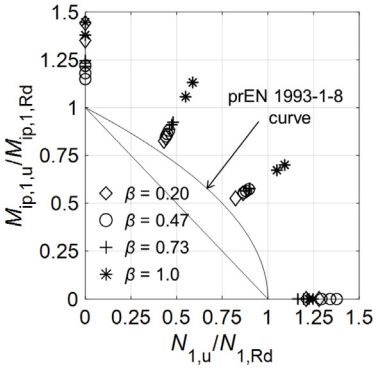

(c) T-joints, mild steel

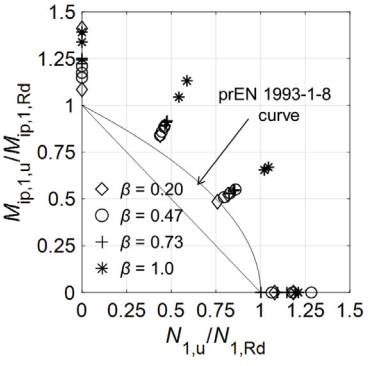

(d) T-joints, high strength steel

Fig. 21. IPB-axial force interactive envelope based on normalization with respect to design resistance of individual loading.

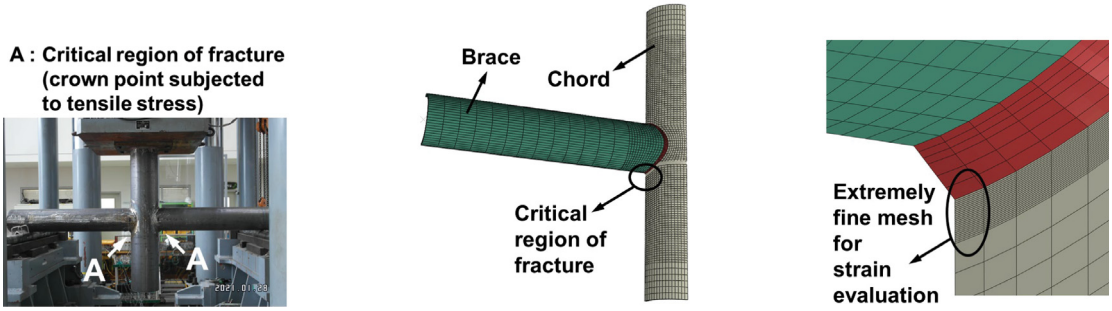

(a) Test specimen C-X-I-700 (b) 1/4 FE model (c) Modeling of critical region

Fig. 22. FE modeling strategy for strain evaluation.

Table 4
FE models for C-X-I-700 (CHS X-joint loaded by IPB).

Model ID	Material	Weld size	Mesh interval at weld toe
FE 1~5	From curved coupon[a]	As measured[c]	For each 5 models, 1/4, 1/8, 1/16, 1/32, $1/64t_0$
FE 6~10	From curved coupon[a]	AWS prequalified weld[d]	
FE 11~15	From weld coupon[b]	AWS prequalified weld[d]	

[a]Curved coupon: $f_{ym} = 761.5$ MPa, $f_{um} = 834.2$ MPa.
[b]Weld coupon: $f_{ym} = 647.0$ MPa, $f_{um} = 719.7$ MPa.
[c]Measured weld size: $w_{leg1} = 2.62$, $w_{height1} = 1.62$, $w_{leg2} = 2.01$, $w_{height2} = 0$, $t_1 = 10.1$ mm ($w_{height2}$ was not measured and assumed from photos taken from the testing. See Fig. 25 for the definitions of the weld size parameters).
[d]AWS prequalified weld: $w_{leg1} = 1.5$, $w_{height1} = 1.0$, $w_{leg2} = 1.5$, $w_{height2} = 0$, $t_1 = 10.1$ mm.

4. Evaluation of strain limit approach

4.1. Mesh sensitivity study

Before evaluating the 5% strain limit approach [6], first a mesh sensitivity study was conducted to identify the element size required to obtain reliable strain values from FE analysis.

Fig. 22 shows a special FE modeling strategy adopted for the IPB-loaded CHS-to-CHS joint specimen C-X-I-700 which was reported in Section 3.3 (see Figs. 14–15). As can be seen in Fig. 22(c), extremely fine meshes were used for the potential cracking region where critical strain should be measured. The critical region was near the crown point of test C-X-I-700. It was expected that exceedingly smaller elements would be required to obtain stable and converged strains from FE analysis compared to the case to predict global responses such as joint load-deformation relationship. Parts away from the critical region were modeled with elements in moderate sizes (approximately $d_0/20$) to ensure accurate load-deformation relationship.

Mesh sensitivity study was done by changing only the mesh size of the critical region while the elements in the remaining parts were kept unchanged. Table 4 presents the FE models used for the simulation of the C-X-I-700 testing. Two material properties and two weld sizes were included.

The reason for considering two different material properties was that in the coupon test, the steel used for the test specimen (ATOS80) showed substantial degradation after welding (see Figs. 23–24). The material properties of the chord near the weld toe was thought to be close to the weld coupon while the chord far from the joint was thought to be more related to the curved coupon (the tube was cold-formed). Therefore, two stress–strain curves from the curved and welded coupons were taken into account. The chord material properties were also applied to the weld. Although the weld material may have non-negligible effect on the strain distribution near the joint, separate consideration of chord and weld materials was not tried because it would complicate the modeling and not be favored in FE-based design.

For the weld size, although it was measured before the testing, the measurement was somewhat imprecise because the profile of the weld toe was not clear. A prequalified weld size specified in AWS D1.1 [32] was also included as well to check the effect of weld size on the joint behavior. Weld parameters for CHS-to-CHS joints (full penetration) are defined in Fig. 25.

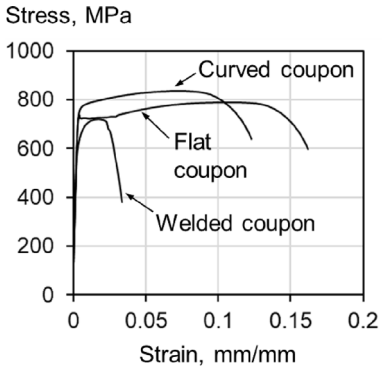

Fig. 23. Stress strain curves of ATOS80 steel.

As shown in Table 4, three groups of FE models were considered based on different materials and weld sizes. In each analysis group, five FE models were constructed with different mesh intervals at the critical region (see Fig. 22(c)): 1/4, 1/8, 1/16, 1/32, and $1/64t_0$, where t_0 is the chord thickness.

In Fig. 26, the load–displacement diagrams obtained from the FE models are presented and compared with the experimental curve. It is noteworthy that the mesh interval at the critical region has no effect on the curve, because the mesh intervals considered are far smaller than the element size required for the convergence of load–displacement relationship. Difference between the curves of FE 1~5 and FE 6~10 indicates that the effect of weld size on joint strength is non-negligible. Difference between FE 6~10 and 11~15 can be attributed to the difference in stress–strain diagrams of the curved and welded coupons (see Fig. 23). The experimental load–displacement curve shows a good agreement with those from FE models 11~15 which employed the

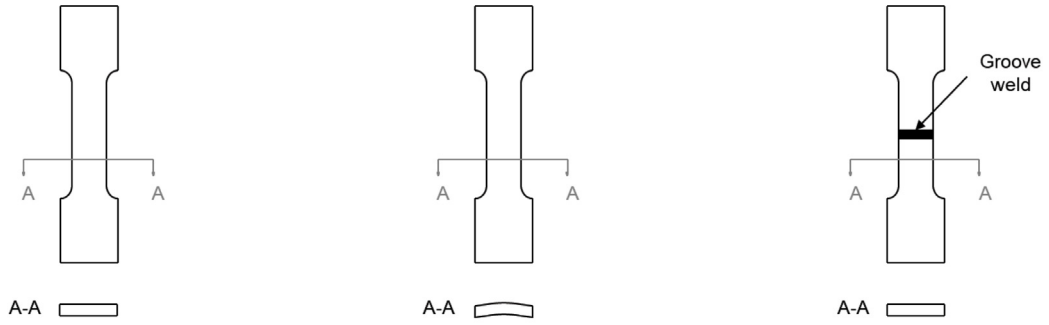

(a) Flat coupon (b) Curved coupon (c) Welded coupon

Fig. 24. Types of coupons considered for ATOS80.

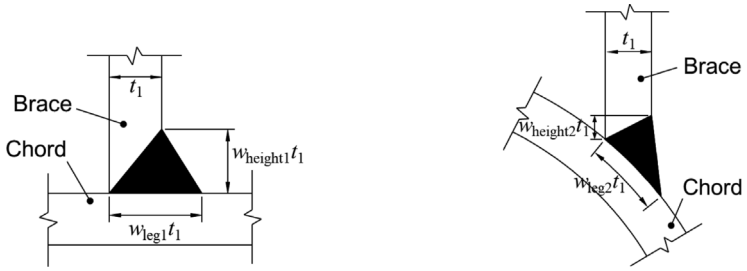

(a) At crown point (b) At saddle point

Fig. 25. Weld parameters for CHS-to-CHS connections (full penetration).

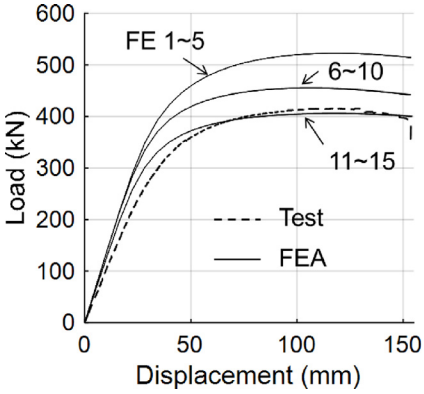

Fig. 26. Load–displacement curves of C-X-I-700 and its FE models.

material properties of welded coupon and the AWS prequalified weld detail.

Strain near the weld toe was evaluated from the FE models following the procedure described in Fig. 27. First, an element is selected along the line of strain evaluation (Fig. 27(a–b)). Because 20-node elements with reduced integration were utilized for the FE models, each element has eight integration points. Therefore, from the element selected in Fig. 27(b), two isoparametric planes can be found which have four integration points each (Fig. 27(c)). The principal strains at points A and B can be found by extrapolating the strains at integration points. Fig. 27(d) shows four integration points G1~G4 and the measuring point A on plane *a*. The principal strain at A (ε_A) is obtained from the principal strains at G1~G4 (ε_1~ε_4) as follows:

$$\varepsilon_A = \sum_{i=1}^{4} \varepsilon_i f_i = \sum_{i=1}^{4} \varepsilon_i \frac{(\xi_A + \xi_i)(\eta_A + \eta_i)}{4\xi_i \eta_i} \tag{21}$$

where f_i (f_1~f_4) is the shape function associated with each integration point. The isoparametric coordinates of A and G1~G4 are given as:

$$(\xi_A, \eta_A) = (1, 1), (\xi_1, \eta_1) = (-\frac{1}{\sqrt{3}}, -\frac{1}{\sqrt{3}}), (\xi_2, \eta_2) = (\frac{1}{\sqrt{3}}, -\frac{1}{\sqrt{3}}),$$
$$(\xi_3, \eta_3) = (\frac{1}{\sqrt{3}}, \frac{1}{\sqrt{3}}), (\xi_4, \eta_4) = (-\frac{1}{\sqrt{3}}, \frac{1}{\sqrt{3}}). \tag{22}$$

The strain at point B can also be calculated in the same manner. Strains at two points are obtained per element along the line of strain evaluation, and as shown in Fig. 27(e), the distribution of principal strain can be obtained over the distance from the weld toe. Linear interpolation is used if the strain needs to be evaluated at a point between two calculation points.

Fig. 28 shows the principal strain distributions obtained from the FE analyses of C-X-I-700. Because the crack initiated at the displacement of 130 mm in the testing, the strain distribution was also evaluated at the same displacement. Overall distribution is shown in Fig. 28(a–c) and the same graphs are enlarged in Fig. 28(d–f) to check the strain at a stand-off distance of $0.5t_0$ (= 5.05 mm). The graphs are separately given for each analysis group (FE 1~5/6~10/11~15, see Table 4).

Comparing different analysis groups in Fig. 28(a–c) clearly indicates that the strain magnitude at small distance (say, 0~3 mm from the weld toe) exhibits higher variability. This means that the strain in the region very close to the weld toe is highly sensitive to the weld size and material properties used for the chord. The stand-off distance, at which the strain limit is imposed, need to be placed away from the high variability region near the weld toe, but also not too far from the weld toe. The distance $0.5t_0$ appears to be an appropriate choice as the stand-off distance in terms of the magnitude and variability of the strain.

Mesh sensitivity of the strain at $0.5t_0$ stand-off distance can be checked in Fig. 28(d–f). Convergence seems to be reached at the third model in each analysis group (FE 3, 8, 13), indicating that the mesh interval should be $1/16t_0$ or smaller for the region of strain calculation.

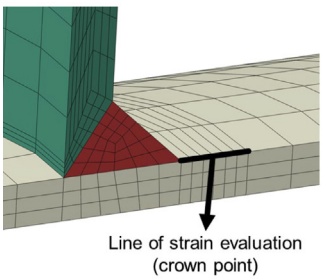

(a) Target location of strain evaluation

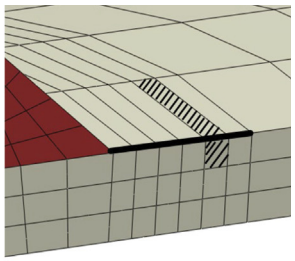

(b) Selecting an element (dashed)

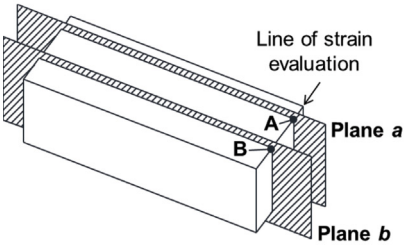

(c) Two isoparametric planes having four integration points each

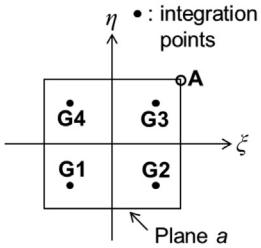

(d) Strain extrapolation to point A

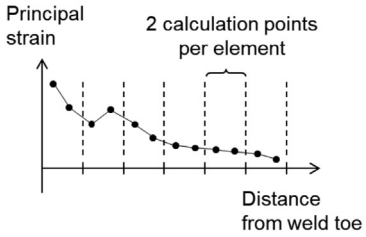

(e) Obtaining principal strain distribution

Fig. 27. Procedure for strain evaluation implemented.

Table 5
FE models for C-XP2-I-460 (branch plate-to-CHS XP-joint loaded by IPB).

Model ID	Edge detail	Weld size	Mesh interval at weld toe
FE 1~5	Square edge	As measured[a]	For each 5 models,
FE 6~10	Chamfer edge	As measured[a]	1/4, 1/8, 1/16, 1/32,
FE 11~15	Chamfer edge	Minimum weld size[b]	$1/64t_0$

(Note) Material properties for the chord: $f_{ym} = 609.0$ MPa and $f_{ym} = 672.1$ MPa.
[a]Measured weld size: $w_{leg1} = 0.60$, $w_{height} = 0.50$, $w_{leg2} = 0.72$, $t_1 = 30.0$ mm (w_{height} was not measured and assumed from photos taken from the testing. See Fig. 30(c–d) for the definitions of the weld size parameters).
[b]Minimum weld size: $w_{leg1} = 0.25$, $w_{height} = 0.50$, $w_{leg2} = 0.50$, $t_1 = 30.0$ mm.

Mesh sensitivity study was further conducted with the test data of C-XP2-I-460, the IPB-loaded longitudinal plate-to-CHS XP joint reported in Section 3.3. In the laboratory testing, the connection underwent substantial deformation and failed by chord punching shear at the weld toe (see Fig. 15).

Table 5 presents the FE models used for the simulation of C-XP2-I-460 testing. Different weld geometries were considered for the three analysis groups, and each analysis group included five FE models with different mesh intervals at the strain evaluation region. An example of FE model is presented in Fig. 29. The weld geometry of the plate connection was represented by the edge detail and weld size, as illustrated in Fig. 30.

At the corners of the weld path, both square edge and rounded edge are common. To facilitate the modeling, a chamfer edge was included instead of the rounded edge. The two edge details applied to the FE models are shown in Fig. 30(b). Fig. 30(c–d) show the parameters used to define the size of the weld. Although the weld size was measured before the testing, the measurement was somewhat imprecise because the profile of the weld was not clear. Considering that the actual weld size might have been overestimated, some FE models were built with a minimum weld size which corresponds to the case when the total length of the weld legs is equal to the thickness of the branch plate, i.e., $2w_{leg2} = 1.0$ in Fig. 30(d) (FE 11~15). The other models were constructed based on the measured weld size (FE 1~5 and 6~10). The material used for the chord was a 460-grade steel SM460 with $f_{ym} = 609.0$ MPa and $f_{ym} = 672.1$ MPa.

In Fig. 31, the load–displacement curves from the FE models of C-XP2-I-460 are presented and compared with that from the experiment. FE models from the same analysis group (i.e., FE 1~5/6~10/11~15) produced almost identical curves, indicating that the element sizes in the models are sufficiently small such that the convergence in terms of load–displacement relationship can be assured. The slight non-convergence at the very tail of the curves was regarded as unimportant.

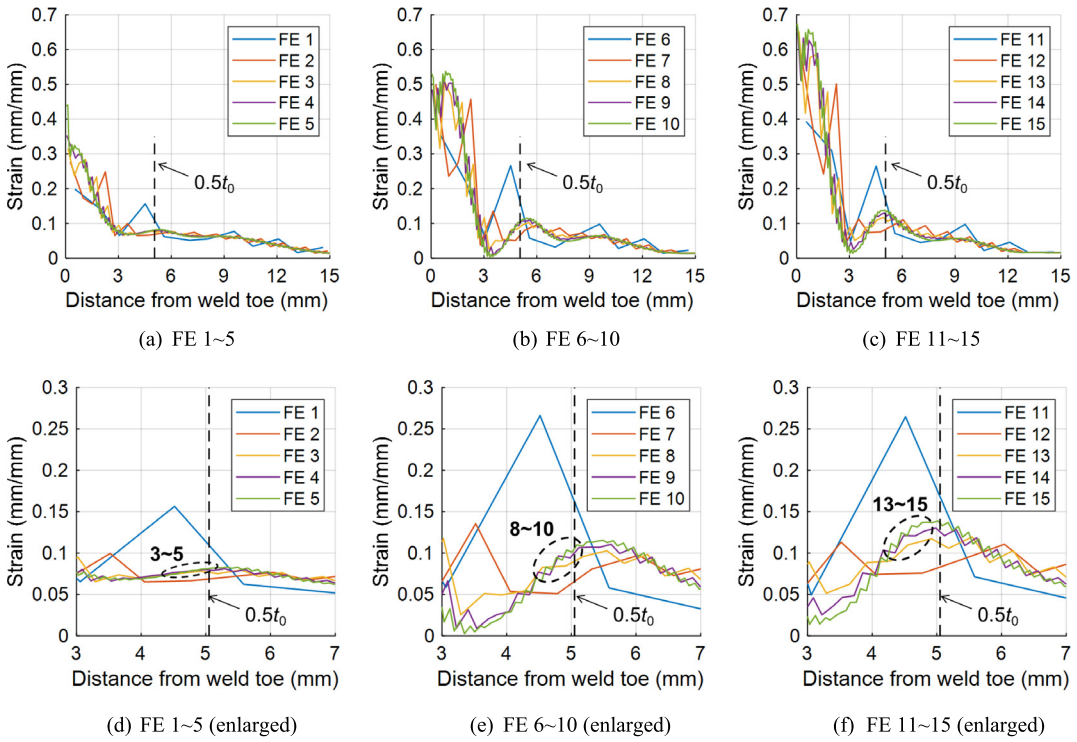

Fig. 28. Principal strain distribution near the weld toe (C-X-I-700 FE models, when the displacement at loading point reaches 130 mm).

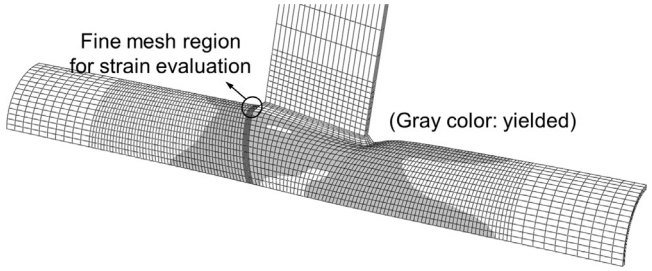

Fig. 29. FE model of C-XP2-I-460 (FE 1, 1/4 model).

It is seen that the joint strength can be greatly affected by the weld geometry. FE models with minimum weld size and round (chamfer) weld profile (FE 11~15) yielded the best agreement with the experimental load–displacement diagram.

Principal strain distribution of C-XP2-I-460 estimated from the FE analyses is presented in Fig. 32. Strains were calculated following the procedure of Fig. 27. The fracture commenced at the displacement of 160 mm in the testing, and based on this, the strain distribution was also obtained at the same displacement. Overall distribution of strain is shown in Fig. 32(a–c), and the same graphs are enlarged in Fig. 32(d–f) to check the strain at a stand-off distance $0.5t_0$ (= 4.7 mm). The graphs are separately given for each analysis group (FE 1~5/6~10/11~15).

Being consistent with the observation made from Fig. 28(a–c) for the CHS-to-CHS joint, Fig. 32(a–c) indicate that for the plate-to-CHS joint too, the magnitude of strain shows high variability at small distances from the weld toe. The distance $0.5t_0$ again appears to be an appropriate choice for the stand-off distance at which the strain limit is imposed.

Mesh sensitivity of the strain at $0.5t_0$ stand-off distance can be checked in Fig. 32(d–f). Similar to Fig. 28(d–f), it is again observed that the mesh interval should be $1/16t_0$ or smaller in the strain calculation region.

4.2. Evaluation of 5% strain limit and proposed modification

Fig. 33 shows the increase of strain at the $0.5t_0$ stand-off distance as the displacement at the loading point increases (i.e., as the joint deformation increases). For each test specimen (C-X-I-700 or C-XP2-I-460), among the fifteen FE models (see Tables 4–5), only three models with the finest mesh interval $1/64t_0$ (FE 5, 10, 15) are presented in Fig. 33. In Fig. 33(a), in the case of all three FE models, 5% principal strain is reached well before the displacement corresponding to the onset of fracture identified from the experiment (130 mm). Therefore, the 5% limiting strain appears to be acceptable as a fracture limiting criterion of test C-X-I-700. On the contrary, in Fig. 33(b), 5% principal strain is not reached in one model (FE 10). Thus, for test C-XP2-I-460, the limiting strain needs to be lower than 5%. It is temporarily suggested that under the IPB loading, 5% strain limit be applied to CHS-to-CHS joints and 2.5% strain limit to plate-to-CHS joints.

The suggested principal strain limits, i.e., 5% for CHS-to-CHS and 2.5% for plate-to-CHS joints, are compared with the deformation limits in Fig. 34. Two deformation limits were included: 3% deformation limit and the rotation angle limit proposed in this paper (Eq. (5)). For each test specimen (C-X-I-700 or C-XP2-I-460), among the fifteen FE models (see Tables 4–5), only three models with the finest mesh interval $1/64t_0$ (FE 5, 10, 15) were considered in Fig. 34.

Three limit points marked in each curve of Fig. 34(a) to (f) are those estimated from the FE analyses. For example, in Fig. 34(a), the ultimate displacement corresponding to each ultimate limit (strain or deformation limit) was obtained from the FE 5 model of C-X-I-700. Then, the three points corresponding to the three ultimate displacements were marked on the experimental load–displacement curve of

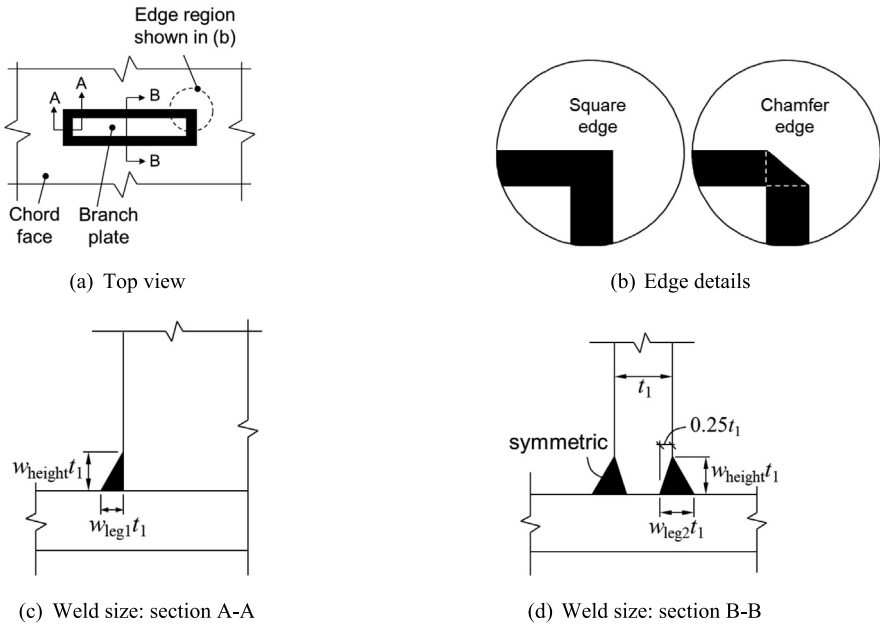

(a) Top view (b) Edge details

(c) Weld size: section A-A (d) Weld size: section B-B

Fig. 30. Weld parameters for plate-to-CHS connections (partial penetration).

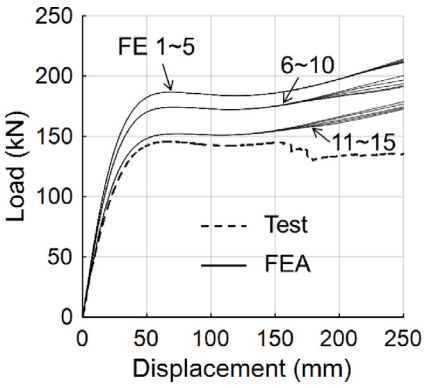

Fig. 31. Load–displacement curves of C-XP2-I-460 and its FE models.

C-X-I-700. Overall, in all Fig. 34(a–f), the joint strengths determined by different ultimate limits show little difference. This indicates that the strain limit may be utilized as an alternative to the deformation limit. The utility of the strain limit as an alternative to deformation limit has also been demonstrated by Kožich et al. (2019) [6].

In Figs. 35–36, further validation was made to the strain limit using the test database. One CHS T-joint loaded by IPB was found from Hu et al. (2021) [28] and two (nominally identical) CHS X-joints loaded by IPB were found from Varelis et al. (2020) [27]. These joints were made of high strength steels and failed by fracture in the chord near the weld toe at the crown point. Unfortunately, no relevant data was available for plate-to-CHS joints subjected to IPB loading.

Table 6 shows the details of the FE models used for the simulation of test data from Hu et al. [28] and Varelis et al. [27]. Two different weld sizes (as measured or as per the AWS prequalified detail) were considered for the test specimen T12, but only the AWS prequalified weld detail was employed for T1 and T2 because measured weld size was not reported. It is observed in Figs. 35–36 that the strain limit gives a reasonable ultimate joint strength comparable to the deformation limits and, at the same time, it is located well before the occurrence of fracture. It should be noted that a matching electrode was used for T1 while an overmatching electrode was used for T2. Because overmatching welding is not common for high strength steel joints, the somewhat lower ductility of T2 is less likely to occur in practice. Except for T2, the strain limit appears to provide sufficient reserve deformation before fracture.

5. Summary and conclusions

In this study, new recommendations were proposed for the deformation and strain limit for high-strength steel circular hollow section (CHS) joints subjected to in-plane bending loading. The proposed recommendations were evaluated by using both finite element analysis results and relevant test data. The results of this study are summarized as follows.

(i) It was shown that existing deformation limits, which have been developed and applied primarily for mild steel joints, may be modified to include high strength steel joints. A joint rotation angle-based deformation limit was newly suggested which allows less deformation to less ductile high strength steel joints.

(ii) Based on the proposed deformation limit, the design resistance, material factor, and design interaction envelope specified in prEN 1993-1-8:2021 were evaluated and they were shown to be appropriate also for high strength steel CHS X and T joints loaded by in-plane bending or combined axial compression and in-plane bending.

(iii) The 5% principal strain limit recently advocated by the revised draft of ISO 14346 was evaluated to be acceptable for CHS-to-CHS joints loaded by in-plane bending (up to grade 700). However, for longitudinal branch plate-to-CHS joints loaded by in-plane bending (up to steel grade 460), a lower limiting strain seems desirable and 2.5% principal strain was temporarily suggested.

(iv) To ensure the convergence of the strain evaluated from finite element analysis, the mesh interval should be $1/16t$ or smaller in the direction of the principal strain (t = thickness of the tubular member to be considered). The mesh interval of $1/16t$ is only required at critical regions in the vicinity of the weld toe. For the rest of the finite

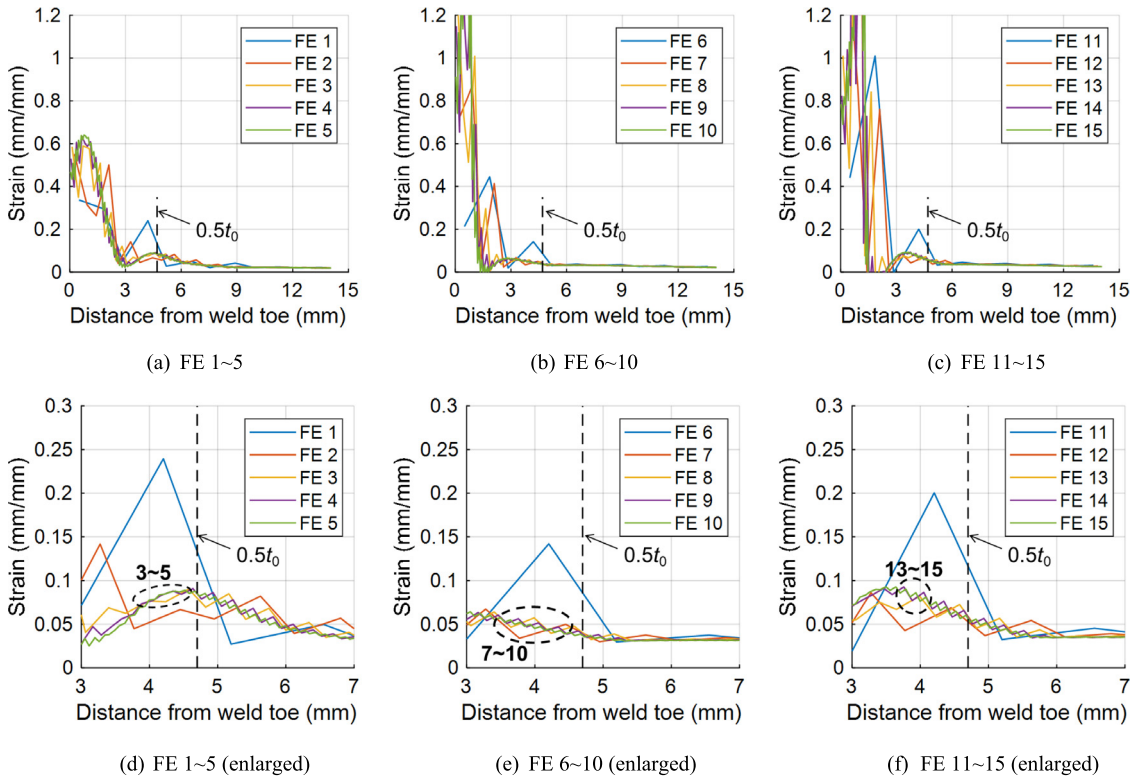

(a) FE 1~5 (b) FE 6~10 (c) FE 11~15

(d) FE 1~5 (enlarged) (e) FE 6~10 (enlarged) (f) FE 11~15 (enlarged)

Fig. 32. Principal strain distribution near the weld toe (C-XP2-I-460 FE models, when the displacement at loading point reaches 160 mm).

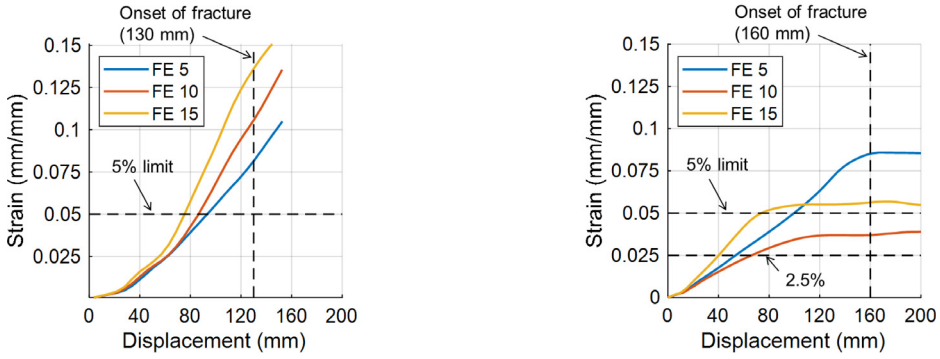

(a) C-X-I-700 (CHS-to-CHS) (b) C-XP2-I-460 (plate-to-CHS)

Fig. 33. Principal strain at $0.5t_0$ stand-off distance.

Table 6
FE models for test specimens reported by Hu et al. (2021) and Varelis et al. (2020).

Test specimen	Joint type	Chord material	FE model (ID)	Weld modeling
T12 (Hu et al. 2021) [28]	CHS T (IPB)	f_{ym} = 761.5 MPa f_{um} = 834.2 MPa	FE 1 FE 2	Using measured dimensions[b] AWS prequalified weld[c]
T1 and T2[a] (Varelis et al 2020) [27]	CHS X (IPB)	f_{ym} = 746 MPa f_{um} = 821 MPa	FEA	AWS prequalified weld[d]

(Note) The mesh interval in the strain evaluation region (at crown point) was $1/64t_0$.
Chord thickness t_0: 9.9 mm (T12), 12.49 mm (T1&T2).
[a]T1 and T2: Two nominally identical specimens.
[b]w_{leg1} = 1.90, $w_{height1}$ = 1.35, w_{leg2} = 1.87, $w_{height2}$ = 0.253, t_1 = 9.9 mm (definition of the symbols can be found in Fig. 25).
[c]w_{leg1} = 1.5, $w_{height1}$ = 1.0, w_{leg2} = 1.5, $w_{height2}$ = 0, t_1 = 9.9 mm.
[d]w_{leg1} = 1.5, $w_{height1}$ = 1.0, w_{leg2} = 1.5, $w_{height2}$ = 0.284, t_1 = 10.27 mm.

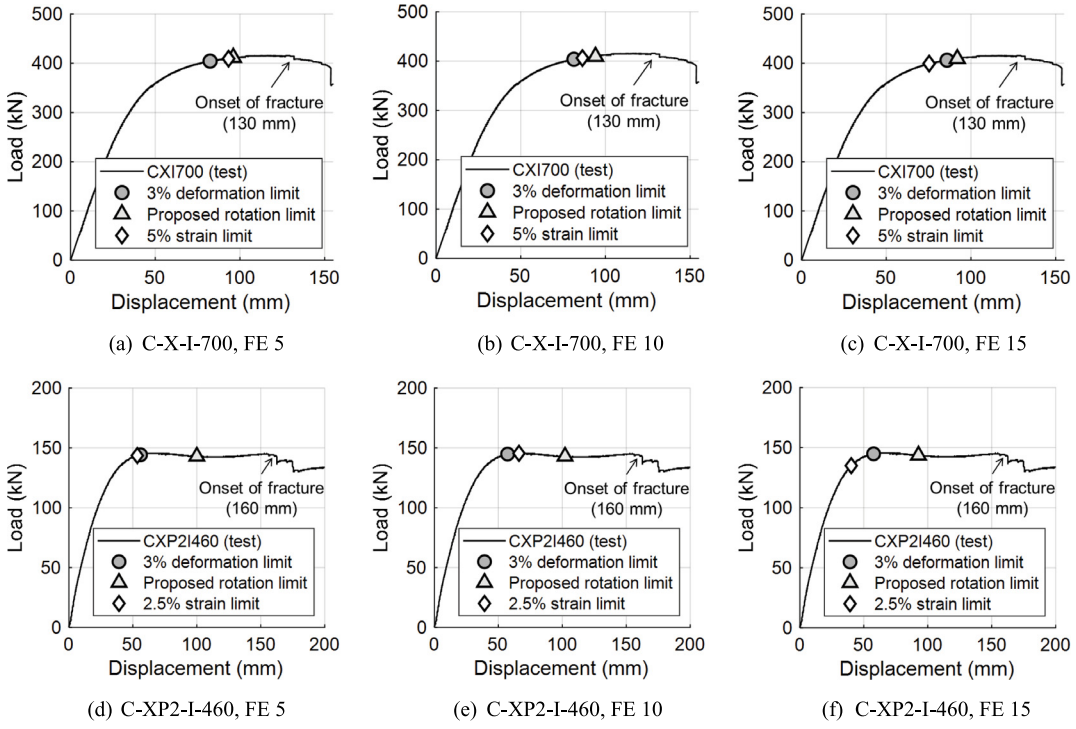

(a) C-X-I-700, FE 5 (b) C-X-I-700, FE 10 (c) C-X-I-700, FE 15

(d) C-XP2-I-460, FE 5 (e) C-XP2-I-460, FE 10 (f) C-XP2-I-460, FE 15

Fig. 34. Deformation and strain limits estimated from FE analysis.

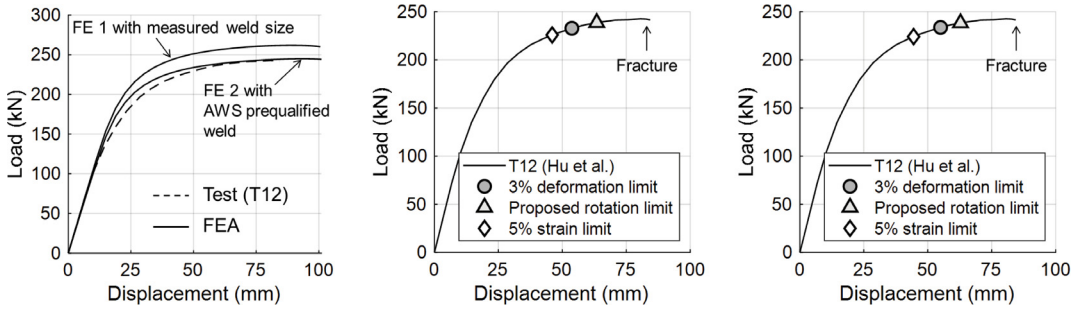

(a) Calibration of load-displacement diagram

(b) Estimated deformation and strain limits from FE 1 (measured weld size)

(c) Estimated deformation and strain limits from FE 2 (AWS prequalified weld)

Fig. 35. Evaluation of strain limit using test data of Hu et al. (2021) [28].

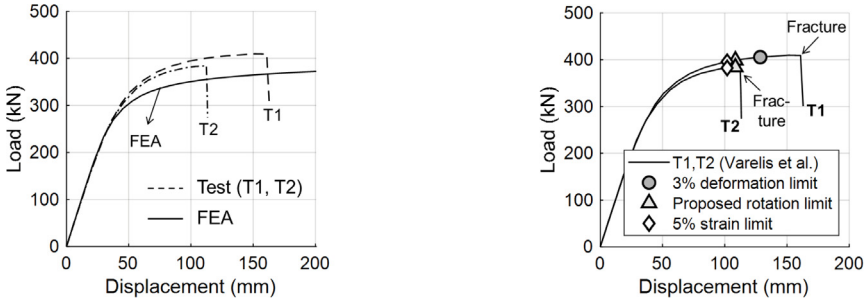

(a) Calibration of load-displacement diagram

(b) Estimated deformation and strain limits from FE analysis (AWS prequalified weld)

Fig. 36. Evaluation of strain limit using test data of Varelis et al. (2020) [27].

element model, typical element size, needed for the convergence of load-deformation relationship, is sufficient.

Notation

Symbol	Definition
b_0	Chord diameter
b_1	Brace diameter
C_f	Material factor
E	Young's modulus
f_i	Shape function associated with ith integration point (i = 1∼4).
f_u	Ultimate (tensile) stress
f_{u0}	Chord ultimate stress
f_{um}	Measured ultimate stress
f_{un}	Nominal ultimate stress
f_y	Yield stress
f_{y0}	Chord yield stress
f_{ym}	Measured yield stress
f_{yn}	Nominal yield stress
f_{ys}	Increased yield stress over the strengthened length
h_1	Height (width) of longitudinally connected branch plate
L_0	Chord length
L_{end}	Strengthened length
l_1	Clear distance between chord face and brace loading point (arm length for IPB loading)
M_c	Compensating end moment
M_{int}	Internal bending moment
$M_{ip,1}$	In-plane bending (IPB) moment
$M_{ip,1,Ed}$	Design IPB load
$M_{ip,1,m}$	Mean IPB strength
$M_{ip,1,Rd}$	Design IPB resistance
$M_{ip,1,u}$	Ultimate IPB strength
$M_{ip,1,u,pure}$	Ultimate strength under pure moment loading
M_{peak}	Peak moment load
M_u	Ultimate strength under pure moment loading (= $M_{ip,1,u,pure}$)
M_{uc}	Ultimate moment strength under combined axial and moment loading
N	Joint load
N_1	Joint axial load
$N_{1,Ed}$	Design axial load
$N_{1,m}$	Mean axial strength
$N_{1,Rd}$	Design axial resistance
$N_{1,u}$	Ultimate axial strength
$N_{1,u,pure}$	Ultimate strength under pure axial loading
N_{peak}	Peak axial load
N_u	Ultimate strength under pure axial loading (= $N_{1,u,pure}$)
N_{uc}	Ultimate axial strength under combined axial and moment loading
Q_f	Chord stress function
t	Thickness
t_0	Chord thickness
t_1	Brace thickness
u	Displacement in the direction perpendicular to the chord connecting face
$W_{pl,H}$	Plastic work done in high strength steel joints
$W_{pl,M}$	Plastic work done in mild steel joints
α	Chord length-to-radius ratio
β	Brace-to-chord diameter ratio
γ	Chord radius-to-thickness ratio
γ_{M5}	Partial safety factor for tubular joints
Δ	Measured displacement
Δ_{def}	Brace deflection component of measured displacement
Δ_{rot}	Joint rotation component of measured displacement
δ	Joint deformation
δ_{avg}	Average joint indentation
δ_y	Effective yielding deformation
δ_u	Ultimate deformation
ε_i	Principal strain at ith integration point (i = 1∼4).
η	Branch plate height to chord diameter ratio
η_i	Isoparametric y-axis of ith integration point (i = 1∼4).
θ_1	Brace angle
ξ_i	Isoparametric x-axis of ith integration point (i = 1∼4).
τ	Brace (or branch plate) thickness to chord thickness ratio
φ	Joint rotation angle
φ_{lim}	Joint rotation angle limit
φ_u	Ultimate joint rotation angle

CRediT authorship contribution statement

Seon-Hu Kim: Writing – original draft, Software, Methodology, Investigation, Conceptualization. **Cheol-Ho Lee:** Writing – review & editing, Supervision, Funding acquisition. **Sang-Hui Han:** Visualization, Investigation, Conceptualization. **Jaap Wardenier:** Writing – review & editing, Supervision.

Declaration of competing interest

The authors declare that they have no known competing financial interests or personal relationships that could have appeared to influence the work reported in this paper.

Data availability statement

Some or all data, models, or code that support the findings of this study are available from the corresponding author upon reasonable request.

Acknowledgments

The authors are grateful for and acknowledge the support of the POSCO Affiliated Research Professor Program for this study.

References

[1] J. Wardenier, Y. Kurobane, J.A. Packer, G.J. Van der Vegte, X.L. Zhao, Construction with Hollow Steel Sections – No. 1: Design Guide for Circular Hollow Section (CHS) Joints under Predominantly Static Loading, second ed., CIDECT, 2008.
[2] J.A. Packer, J. Wardenier, X.L. Zhao, G.J. van der Vegte, Y. Kurobane, Design guide for rectangular hollow section (RHS) joints under predominantly loading, in: CIDECT Design Guide (3), second ed., CIDECT, Geneva, Switzerland, 2009.
[3] L.H. Lu, G.D. de Winkel, Y. Yu, J. Wardenier, Deformation limit for the ultimate strength of hollow section joints, in: Proc. 6th Intl. Symp. on Tubular Structures, Tubular Structures VI, 1994, pp. 341–347.
[4] C.H. Lee, S.H. Kim, D.H. Chung, D.K. Kim, J.W. Kim, Experimental and numerical study of cold-formed high-strength steel CHS X-joints, J. Struct. Eng. ASCE 143 (8) (2017) 04017077.
[5] X.-L. Zhao, J. Wardenier, J.A. Packer, G.J. van der Vegte, Current static design guidance for hollow-section joints, Struct. Build. 163 (SB6) (2010) 361–373.
[6] M. Kožich, P. Jehlička, F. Wald, X.D. Bu, J.A. Packer, J. Kabeláč, Towards establishing a design resistance for hollow section joints, in: Proc. the 17th Int'l Symposium on Tubular Structures, Tubular Structures XVII, Singapore, 2019, pp. 643-650.
[7] J.A. Packer, FE-Based Design of HSS Connections, Steel Tube Institute, 2020.
[8] IIW, Draft of ISO 14346: Static Design Procedure for Welded Hollow-Section Joints – Recommendations, IIW Doc. XV-E-497F-21, International Institute of Welding, 2021.
[9] J.A. Yura, N. Zettlemoyer, I.F. Edwards, Ultimate capacity equations for tubular joints (OTC 3690), in: Proc. 12th Annual Offshore Technology Conf. Houston, TX, 1980.

[10] L.H. Lu, J. Wardenier, Ultimate deformation criteria for uniplanar connections between I-beams and RHS columns under in-plane bending, in: Proc. the Fourth Int Offshore and Polar Engineering Conf. Osaka, Japan, 2004.
[11] Y. Yu, The Static Strength of Uniplanar and Multiplanar Connections in Rectangular Hollow Sections (Ph.D. dissertation), Delft Univ. Of Technology, Delft, The Netherlands, 1997.
[12] X.D. Qian, Static Strength of Thick-Walled CHS Joints and Global Frame Behavior (Doctoral dissertation), National University of Singapore, 2005.
[13] S.-H. Kim, C.-H. Lee, Static behaviour of high-strength steel CHS T-joints under in-plane moment loading, in: Proc. the Ninth European Conference on Steel and Composite Structures (Eurosteel 2020) (Held Virtually), The University of Sheffield, 2021.
[14] CEN, Eurocode 3: Design of Steel Structures – Part 1-5: Plated Structural Elements, EN 1993-1-5, European Committee for Standardization, Brussels, Belgium, 2006.
[15] G.J. Van der Vegte, Y. Makino, J. Wardenier, The effect of chord pre-load on the static strength of uniplanar tubular K-joints, in: Proc. The Twelfth International Offshore and Polar Engineering Conference, Kitakyushu, Japan, 2002.
[16] . Dier, et al., New data on the capacity of X-joints under tension and implications for codes, in: Proc. the ASME 27th Int'l Conf. on Offshore Mechanics and Arctic Engineering (OMAE2008), Estoril, Portugal, 2008.
[17] Simulia, Abaqus 6.14: Abaqus/CAE User's Guide, Simulia, Providence, RI, 2014.
[18] KCSC, KDS 41 31 00:2019, Korean Design Standard (in Korean), Korea Construction Standards Center, Goyang, Korea, 2019.
[19] S.-H. Kim, C.-H. Lee, Experimental investigation of CHS t/y-joints fabricated from high-strength steel, Steel Constr.: Des. Res. 14 (3) (2021) 167–184.
[20] ASTM, StandArd Specification for Cold-Formed Welded and Seamless Carbon Steel Structural Tubing in Rounds and Shapes, A500/A500M-20, American Society for Testing and Materials, Pennsylvania, 2020.
[21] A.P. Voth, J.A. Packer, Branch plate-to-circular hollow structural section connections, I: Experimental investigation and finite-element modeling, J. Struct. Eng. 138 (8) (2012) 995–1006.
[22] CEN, Eurocode 3: Design of Steel Structures – Draft Part 1.8: Design of Joints, prEN 1993-1-8:2021, European Committee for Standardization, Brussels, 2021.
[23] S.-H. Kim, C.-H. Lee, Automatic generation of finite elements for numerical analysis of welded tubular connections, in: Proc. the 11th International Symposium on Steel Structures (ISSS 2021), Jeju, South Korea, 2021.
[24] G.J. Van der Vegte, J. Wardenier, X. Qian, Y.S. Choo, Reanalysis of the moment capacity of CHS joints, in: Proceedings of the 12th International Symposium on Tubular Structures, Tubular Structures XII, Shanghai, China, 2008, pp. 579-588.
[25] S.-H. Han, C.-H. Lee, S.-H. Kim, Chord plastification strength of longitudinal plate-to-CHS joints with steel grade up to 460 MPa under combined axial compression and in-plane bending, J. Construct. Steel Res. 184 (2021) 106804.
[26] S.H. Lee, K.J. Shin, H.D. Lee, W.B. Kim, J.G. Yang, Behavior of plate-to-circular hollow section joints of 600 MPa high-strength steel, Int. J. Steel Struct. 12 (4) (2012) 473–482.
[27] G.E. Varelis, T. Papatheocharis, S.A. Karamanos, P.C. Perdikaris, Structural behavior and design of high-strength steel welded tubular connections under extreme loading, Mar. Struct. 71 (2020) 102701.
[28] Y.F. Hu, K.F. Chung, H. Jin, H. Ban, D.A. Nethercot, Structural behaviour of T-joints between high strength S690 steel cold-formed circular hollow sections, J. Construct. Steel Res. 182 (2021) 106686.
[29] G.J. Van der Vegte, J. Wardenier, X.L. Zhao, J.A. Packer, Evaluation of new CHS strength formulae to design strengths, in: Proceedings of the 12th International Symposium on Tubular Structures, Tubular Structures XII, Shanghai, China, 2008, 313–322.
[30] P.W. Hoadley, J.A. Yura, Ultimate strength of tubular joints subjected to combined loads, in: OTC 4854, Offshore Technololgy Conference, 1985.
[31] P.W. Marshall, Discussion of load interaction in T-joints of steel circular hollow sections by alex stamenkovic and keith d. Sparrow (september, 1983), J. Struct. Eng. 110 (11) (1984) 2817–2818.
[32] AWS, Structural Welding Code – Steel, AWS D1.1/D1.1M, twenty fourth ed., vol. 2020, American Welding Society, Miami, FL.